

Monitoring Nonadiabatic Dynamics of the RNA Base Uracil by UV Pump–IR Probe Spectroscopy

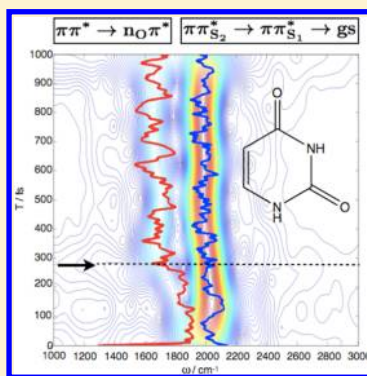
Benjamin P. Fingerhut,* Konstantin E. Dorfman,* and Shaul Mukamel*

Chemistry Department, University of California, Irvine, California 92697-2025, United States

Supporting Information

ABSTRACT: Resolving the excited-state dynamics of DNA and RNA nucleobases has attracted considerable attention. UV irradiation of the isolated nucleobases leads to the population of an electronic excited state, which is quenched by internal conversion mediated by conical intersections on an ultrafast time scale. We present nonadiabatic on-the-fly molecular dynamics simulations of the UV pump–IR probe signal of the pyrimidine nucleobase uracil using a novel semiclassical protocol that takes into account the path integral over the excited-state vibrational dynamics and properly describes the joint temporal and spectral resolution of the technique. Simulations of vibrational motions of carbonyl fingerprint modes in the electronically excited states reveal clear signatures of different relaxation pathways on a time scale of hundreds of femtoseconds, which arise from an ultrafast branching in the excited state. We show that the inherent temporal and spectral resolution of the technique is not purely instrumental but also depends on the vibrational fluctuation time scale.

SECTION: Spectroscopy, Photochemistry, and Excited States



The strong UV absorption bands of DNA and RNA nucleobases lead to the population of bright valence excited states with $\pi\pi^*$ character. The nucleobases have been engineered by nature to be photostable with respect to UV irradiation. At the core of this self-protecting property are few-picosecond excited-state deactivation mechanisms involving conical intersections^{1,2} where electronic energy is very rapidly converted into vibrational energy, allowing to minimize harmful photochemical processes that can eventually lead to DNA photolesions. These damages can be corrected to some extent in enzymatic repair processes, but an accumulation of photolesions leads to genetic mutations and ultimately to diseases like skin cancer. The harmful molecular mechanisms leading to photochemical DNA damage have been shown to occur on the short picosecond time scale,³ thus directly competing with photoprotection mechanisms, and are additionally affected by variations of the base sequence and the double helix conformation.^{4–7}

It is well established that the purine nucleobases adenine and guanine decay with a single quenching mechanism^{8–10} that is mediated by the barrierless access to a seam of conical intersections with the electronic ground state.^{11–14} In contrast, the excited-state lifetimes of the pyrimidine bases are somewhat longer (with the longest for thymine) and involve several interconnected excited-state decay pathways.^{15–17} A direct $\pi\pi^* \rightarrow gs$ channel leads to ultrafast repopulation of the electronic ground state,^{9,10,18,19} while an indirect $\pi\pi^* \rightarrow n_O\pi^* \rightarrow gs$ channel involves an optical dark $n_O\pi^*$ intermediate state with a longer lifetime.¹⁹ Dynamical simulations of DNA and RNA bases helped establish the interconnection between the two relaxation mechanisms and additional minor ring-opening

pathways, but the relative importance of these pathways is still under debate.^{20–22} A clear assignment of spectroscopic signatures of these pathways has only been provided for the earlier stages of the process.²⁰

Commonly applied time-resolved techniques such as UV or visible pump–probe or photoelectron spectroscopy offer a high sub-100 fs temporal resolution.^{9,10} The multidimensional optical counterparts of these techniques have been traditionally developed in the 600–800 nm regime, limited by laser sources, and are now becoming feasible in the UV.^{23–28} The broad bandwidth of the optical or ionizing probe pulses lacks selectivity for the underlying vibrational dynamics. Only the population decay of the bright $\pi\pi^*$ state is captured by probing the system dynamics in the optical regime. These techniques thus fail to directly monitor the population of dark states and to decipher between the particular pathways.

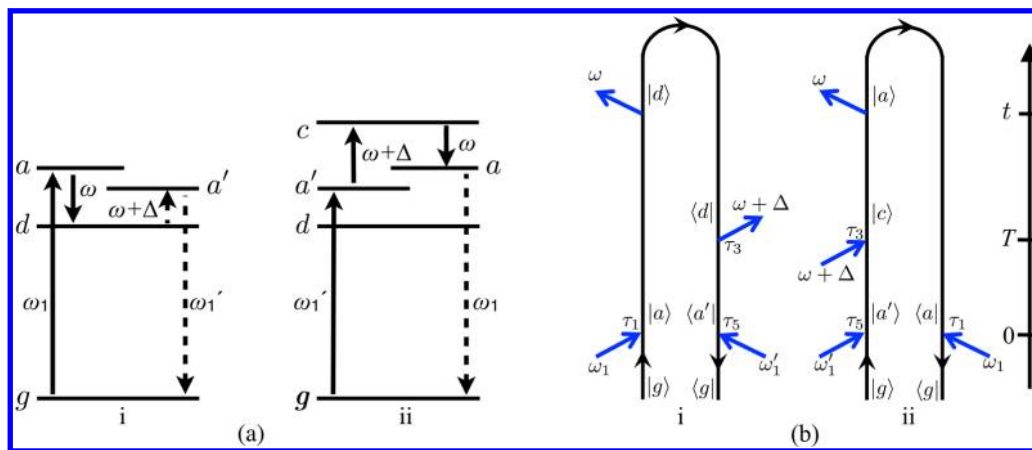
Structural information about the rearrangement of atoms can be derived directly from time- and frequency-resolved vibrational spectroscopy (either with IR or Raman probes). Unique marker bands (e.g., the IR-intense carbonyl C=O stretch vibrations of the nucleobases) serve as fingerprints of the excited-state photoreaction or nonadiabatic relaxation dynamics. This allows one to resolve transient reaction intermediates,^{29–31} obtain structural details,³² and thus ultimately resolve the reaction mechanism.^{3,4,33,34} The UV pump–IR probe technique has been proven to be a valuable direct probe for complex photoreactions by allowing one to identify the real

Received: April 11, 2013

Accepted: May 20, 2013

Published: May 20, 2013



Scheme 1. Time-Resolved Frequency-Dispersed Pump–Probe Spectroscopy^a

^a(a) Schematic of ground and excited states accessed by the pump–probe pulse sequence; solid arrows represent intervals with forward time propagation, and dashed lines represent backward time propagation. (b) Closed-time path loop diagrams that, together with their complex conjugates, represent the pump–probe signal. Diagram (i) stimulated emission and (ii) absorption contribution to the signal; diagram rules are given in ref 43. ω_1 and ω_1' denote interactions with the pump; the corresponding times τ_1 and τ_5 are centered around zero. $\omega + \Delta$ represents an interaction with the probe at time τ_3 that is centered around the pump–probe delay T . Time translational invariance of the matter correlation functions implies that the sum of frequencies in each diagram must be zero, that is $\omega_1 - \omega_1' - \omega + (\omega + \Delta) = 0$ for (i) and $\omega_1 - \omega_1' + \omega - (\omega + \Delta) = 0$ for (ii).

time reaction mechanism leading to the formation of photolesions in DNA nucleobases^{3,4,34,35} and other photo-reactions.^{30,31,33,36}

We present a semiclassical microscopic simulation protocol for the UV pump–IR probe signal of uracil that takes into account the entire path integral of the excited-state dynamics as well as the temporal and spectral profile of the IR probe pulse. The interpretation of these signals requires a careful analysis of the interplay between spectral and temporal resolution in the excited state because time-resolved vibrational spectra^{37–39} may not be simply interpreted as an instantaneous snapshot of the nuclear dynamics;⁴⁰ sums over paths smear the temporal and spectral resolutions. The time-dependent vibrational frequencies (subject to nonadiabatic relaxation) introduce a matter chirp contribution to the signal that affects the effective pulse length for highest temporal resolution. We demonstrate that the resolution in vibrational spectra is governed by both the infrared probe and the underlying matter dynamics and cannot be controlled solely by experimental knobs. The present analysis and the conclusions may be readily extended to a stimulated Raman probe.⁴¹

Our simulations employ nonadiabatic on-the-fly molecular dynamics to calculate the vibrational spectra. A small vibrational system is treated quantum mechanically, whereas a classical bath causes a time-dependent modulation of the system Hamiltonian. The required quantities are directly derived from nonadiabatic mixed quantum–classical dynamics where the excited-state vibrational Hamiltonian is reconstructed on-the-fly by block diagonalization in a mode tracking procedure,⁴² which avoids the calculation of the entire excited-state Hessian matrix. The numerical algorithm developed for the simulation of the time evolution of specific “fingerprint” modes (like, e.g., C=O modes) scales linearly with the number of vibrations, allowing for simulations of medium-sized molecules in the excited states, and numerical effort is decoupled from system size.

We further dissect the contributions of different femtosecond relaxation mechanisms to the signal and predict the signatures of the concurring relaxation pathways, excited-state trapping,

and ultrafast deactivation to the electronic ground state. The spectra show unique signatures from the different deactivation pathways and allow one to assess their relative importance in future experiments.

Loop Diagram Representation of Time- and Frequency-Resolved Pump–Probe Signals. In the UV pump–IR probe technique, the pump pulse \mathcal{E}_1 centered at time zero promotes the system from its ground electronic state g to the vibrational state a of an excited electronic state (see Scheme 1a) and launches the vibrational dynamics. The IR probe \mathcal{E}_2 centered at T can then stimulate either emission that couples the vibrational state a and a lower vibrational state d or absorption to a higher vibrational state c . The complex electric field reads

$$\mathcal{E}(t) = \mathcal{E}_1(t) + \mathcal{E}_2(t - T) \quad (1)$$

The pump–probe signal $S_{\text{PP}}(\omega, T)$ is given by the frequency-gated change in probe intensity and depends parametrically on T . The relevant loop diagrams shown in Scheme 1b (plus their complex conjugates) contain four field–matter interactions, two with each pulse. Diagrams (i) and (ii) correspond to emission and absorption, respectively, of the IR probe pulse. The frequency-gated signal $S_{\text{PP}}(\omega, T) = S_{\text{PP}}^{(i)}(\omega, T) + S_{\text{PP}}^{(ii)}(\omega, T)$ can be directly read off of the diagrams and is given by

$$\begin{aligned} S_{\text{PP}}^{(i)}(\omega, T) = & \mathcal{J} \left[\frac{2}{\hbar} \int_{-\infty}^{\infty} \frac{d\Delta}{2\pi} \int_{-\infty}^{\infty} dt \int_{-\infty}^t d\tau_1 \int_{-\infty}^t d\tau_3 \right. \\ & \times \int_{-\infty}^{\tau_3} d\tau_5 \mathcal{E}_2^*(\omega) \mathcal{E}_2(\omega + \Delta) \mathcal{E}_1^*(\tau_5) \mathcal{E}_1(\tau_1) \\ & \times \langle V_e G^\dagger(\tau_3, \tau_5) V_n G^\dagger(t, \tau_3) V_n G(t, \tau_1) V_e \rangle \\ & \times e^{i\omega(t-\tau_3)-i\Delta(\tau_3-T)} \left. \right] \end{aligned} \quad (2)$$

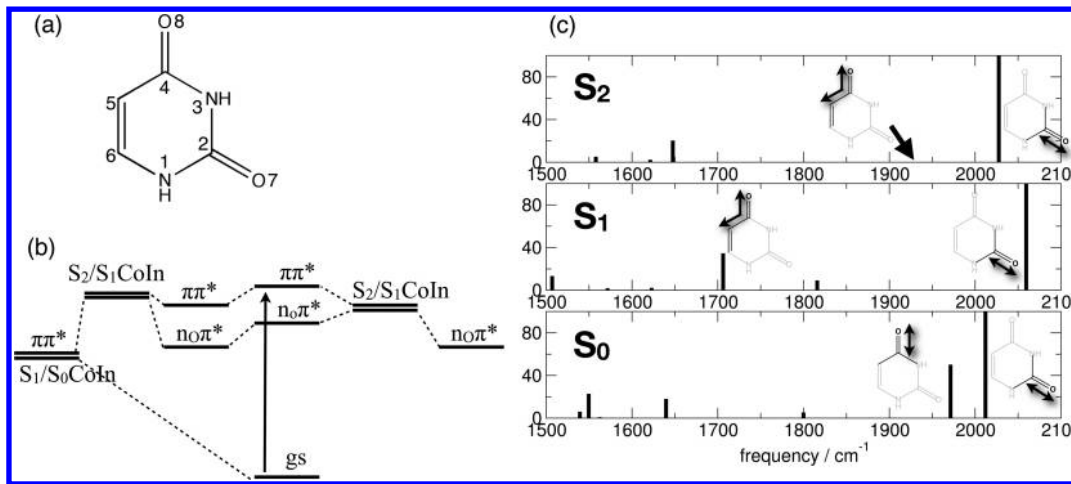


Figure 1. (a) Chemical structure of uracil. (b) Schematic of the femtosecond excited-state relaxation mechanisms. (c) Carbonyl stretch vibrations: frequencies and relative intensities of the carbonyl marker bands in the electronic ground state S_0 ($\tilde{\nu}_{C=O_7} = 2012 \text{ cm}^{-1}$, $\tilde{\nu}_{C=O_8} = 1971 \text{ cm}^{-1}$) and the excited states S_1 ($n_{O_8}\pi^*$; $\tilde{\nu}_{C=O_7} = 2059 \text{ cm}^{-1}$, $\tilde{\nu}_{C=O_8} = 1706 \text{ cm}^{-1}$) and S_2 ($\pi\pi^*$; $\tilde{\nu}_{C=O_7} = 2028 \text{ cm}^{-1}$, $\tilde{\nu}_{C=O_8} = 1929 \text{ cm}^{-1}$).

$$\begin{aligned} S_{pp}^{(ii)}(\omega, T) = & \mathcal{J} \left[\frac{2}{\hbar} \int_{-\infty}^{\infty} \frac{d\Delta}{2\pi} \int_{-\infty}^{\infty} dt \int_{-\infty}^t d\tau_1 \int_{-\infty}^t d\tau_3 \right. \\ & \times \int_{-\infty}^{\tau_3} d\tau_5 \mathcal{E}_2^*(\omega) \mathcal{E}_2(\omega + \Delta) \mathcal{E}_1(\tau_5) \mathcal{E}_1^*(\tau_1) \\ & \times \langle V_e G^\dagger(t, \tau_1) V_n G(t, \tau_3) V_n^\dagger G(\tau_3, \tau_5) V_e^\dagger \rangle \\ & \times e^{i\omega(t-\tau_3)-i\Delta(\tau_3-T)} \end{aligned} \quad (3)$$

where $G(t_1, t_2) = (-i/\hbar)\theta(t_1 - t_2)e^{-iH(t_1-t_2)}$ is the retarded Green's function representing forward propagation from t_1 to t_2 . The advanced Green's function $G^\dagger(t_1, t_2)$ represents backward propagation from t_1 to t_2 , and V_e and V_n denote the electronic and vibrational dipole operators, respectively. The two interactions with the probe involve the detection mode ω and another mode $\omega + \Delta$. The relevant range of the τ_3 integration is controlled by the effective bandwidth of the variable Δ . In both diagrams (i) and (ii), the probe is frequency-dispersed in the detection. Because only a single mode is selected for the detection, one can ask why does the probe duration matter at all? This is apparent from the diagrams that show that the signal involves two interactions with the probe. The frequency-dispersed detection only selects the frequency of the last interaction $\mathcal{E}_2^*(\omega)$, whereas the other interaction $\mathcal{E}_2(\omega + \Delta)$ may still involve many other modes, making the signal dependent on the probe bandwidth and the relative phase of different modes. The time resolution is lost only if the other interaction also selects a single mode and is sharply peaked at $\Delta = 0$. This implies a CW probe. The Δ bandwidth cannot be controlled experimentally because it depends on the system dynamics details.

Semiclassical Approach: Coupling to a Classical Bath. Equations 2 and 3 may be used for a complete-many body propagation of the wave function, which is exact and numerically expensive. The signal is given by a sum over paths spanning both branches of the loop. We shall employ a simplified protocol by treating some of the bath degrees of freedom as classical while retaining the quantum character of selected vibrations^{40,41} (in our case, the IR-intense carbonyl C=O stretch vibrations of the nucleobase). The selected modes are then modulated during the course of the

nonadiabatic dynamics of other classical bath degrees of freedom. We further assume that the preparation pump is impulsive, setting $\mathcal{E}_1(t) = \mathcal{E}_1\delta(t)$ and eliminating the τ_1 and τ_5 integrations in eqs 2 and 3. The semiclassical signal finally reads⁴¹

$$\begin{aligned} S_{pp}(\omega, T) = & -\mathcal{J} \left\langle \frac{2i}{\hbar^4} \int_0^{\infty} d\tau_3 |\mathcal{E}_1|^2 \mathcal{E}_2^*(\omega) \mathcal{E}_2(\tau_3 - T) \right. \\ & \times \int_{\tau_3}^{\infty} dt e^{i\omega(t-T)} \sum_a |\mu_{ag}|^2 e^{-2\gamma_a t} \\ & \times \left. \left(\sum_c |\mu_{ac}|^2 e^{-i\int_{\tau_3}^t \omega_{ca}(t') dt'} + \sum_d |\mu_{ad}|^2 e^{i\int_{\tau_3}^t \omega_{ad}(t') dt'} \right) \right\rangle_e \end{aligned} \quad (4)$$

where $\omega_{ab} \equiv \omega_a - \omega_b$ and γ_a^{-1} is the lifetime of state a. $\langle \dots \rangle_e$ represents the ensemble averaging over a set of classical trajectories. This signal is given by a path integral in the molecule and field space involving the vibrational frequency trajectories $\omega_{ca}(t)$ and $\omega_{ad}(t)$. In addition, the starting point τ_3 is not precisely defined because it is an integration variable. The signal depends not only on the initial and final values of the vibrational frequency $\omega_{ca}(t)$ but rather on the entire pathway from time T to the time when the polarization decays to zero. In time-resolved measurements, the probe must have a broader bandwidth than the inverse time scale of the vibrational dynamics. The latter is given by the spread of transition frequencies $\omega_{a'a}$ (decay of a superposition) and by the dephasing rate γ_a . Even if the probe pulse is impulsive and delayed by T , the pulse may not be simply replaced by the δ function because it can be longer than the infrared period. Thus, an infrared pulse can be at most "semi-impulsive" (i.e., short compared to the vibrational relaxation process but not compared to the period of high-frequency vibrations ~ 2000 – 3000 cm^{-1}). In contrast, the visible pulse used in a stimulated Raman process can be truly impulsive (short compared to the vibrational period).^{41,44–48}

Electronic Relaxation. UV radiation excites the molecule (Figure 1a) to the bright $\pi\pi^*$ S_2 state, which is located 5.07 eV above the S_0 state on MRPT2-CAS(14/10) level of theory and above the dark $n_{O_8}\pi^*$ state (Figure 1b; for a discussion of the electronic excited states and electronic structure methods, see

Supporting Information (SI) Table 1). Figure 1c shows the IR stick spectrum of uracil calculated on the CAS(14/10) level of theory in the electronic ground state S_0 (bottom), the S_1 minimum with $n_O\pi^*$ character (middle), and the S_2 minimum with $\pi\pi^*$ character (top). [The C=O vibrational frequencies are calculated on the CAS(14/10) level of theory (basis: 6-31G*). Due to the lack of dynamic electron correlation and the finite basis size vibrational frequencies appear blue-shifted compared to experiment, comparison with the experimental vibrational spectrum (recorded at low temperatures in an argon matrix)⁴⁹ suggests a scaling factor of ~0.86.] In S_0 , two intense and spectrally isolated C=O stretch vibrations are identified at $\tilde{\nu} = 2012$ and 1971 cm^{-1} ; the splitting is attributed to the different chemical environment in the aromatic π system of uracil. In the $\pi\pi^*$ minimum, the higher-energy C=O₇ mode (where C=O_n is the localized stretch vibration involving atom n) is blue-shifted by ~16 cm⁻¹, and the high oscillator strength of this mode is preserved. Due to the broken aromaticity in the $\pi\pi^*$ state, the low-energy C=O₈ mode is red-shifted by ~41 cm⁻¹, and the oscillator strength is largely diminished, reflecting the population of the antibonding π^* orbital of the C=O₈ bond. Inspection of the normal mode vector shows that the localized C=O₈ mode in S_0 develops into a partially delocalized normal mode whose motion involves the adjacent partial double bond, reflecting the enolat resonance structure of uracil. Nevertheless, both C=O modes remain decoupled. In the S_1 state with $n_O\pi^*$ character, the motion of the C=O₈ mode is even more delocalized, and the energy is further reduced ($\tilde{\nu} = 1719\text{ cm}^{-1}$). The oscillator strength is about 33% of the C=O₇ ground-state vibration. The high-energy C=O₇ mode preserves its localized character and shows a blue shift of ~47 cm⁻¹ compared to the S_0 state.

Figure 2 depicts the time evolution of the excited-state electronic populations within the first picosecond, averaged over 44 trajectories (electronic structure method CAS(14/10); for details of the nonadiabatic on-the-fly molecular dynamics simulations, see the Theoretical Methods section). The molecule starts in the bright $\pi\pi^*$ state (47.6% in S_2 and 52.3% in S_3); within the first 30 fs, the S_2 population is rapidly increased to 86% by following the diabatic character of the $\pi\pi^*$ state. This initial $S_3 \rightarrow S_2$ population transfer is accompanied by a partial population of the S_1 state by ~24% due to $S_2 \rightarrow S_1$ population transfer within the first 50 fs. The S_1 population remains nearly constant until $t = 200$ fs and then increases to ~57% at $t = 1\text{ ps}$. This increase is fed from the S_2 state whose population is reduced by about ~50% in the time interval [200; 1000] fs. Accordingly, the decay of S_2 occurs by two mechanisms, first due to population of the dark S_1 state with $n_O\pi^*$ character and second due to population transfer into the electronic ground state S_0 , which is populated by about 18% at $t = 1000$ fs. Additionally, a significant fraction of the population (about 24%) is trapped in the S_2 state at $t = 1000$ fs. Interestingly, the S_1 population is not transiently increased by the $S_2 \rightarrow S_0$ relaxation.

The typical trajectories depicted in Figure 2b and c demonstrate the two relaxation mechanisms of S_2 (the populated state at time t is highlighted in cyan). Figure 2b shows the population relaxation of the S_2 state leading to a trapped S_1 population. In this trajectory, the S_2/S_1 seam of the conical intersection is reached at $t = 270$ fs. The energy gap between S_1 and S_0 is then reduced, but no hopping event into the ground state occurs, and the trajectory evolves on the dark

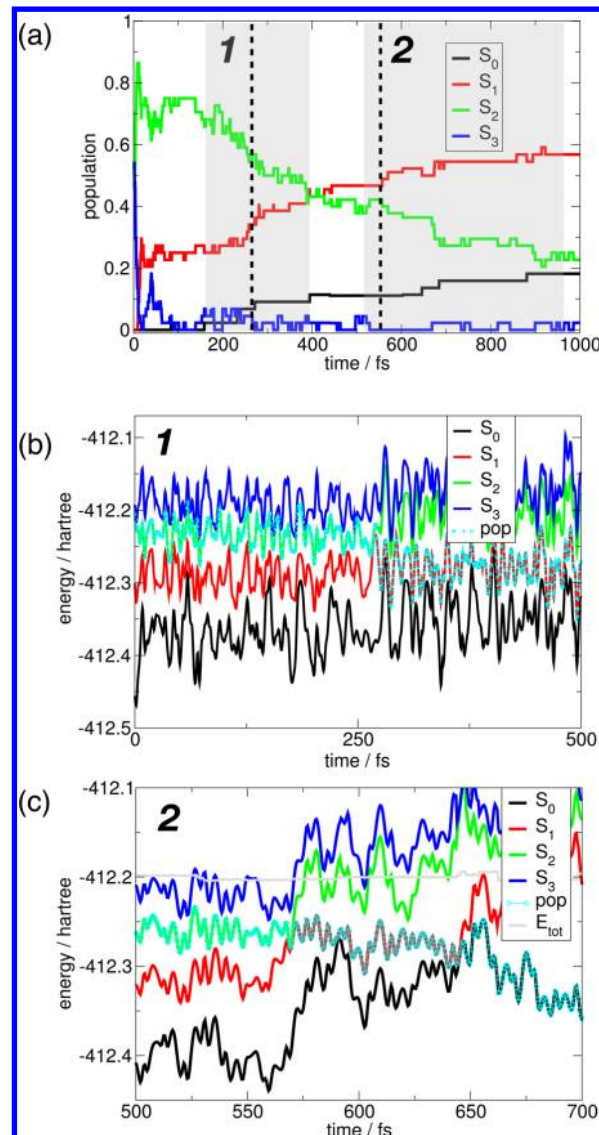


Figure 2. Time evolution of electronic populations and sample trajectories: (a) Mean adiabatic electronic state population averaged over 44 trajectories starting in the bright $\pi\pi^*$ state. Depending on the initial geometry, the initial state is either S_2 (47.7%) or S_3 (52.3%); (b) time evolution of the electronic states for a prototype trajectory showing $\pi\pi^* \rightarrow n_O\pi^*$ relaxation ($S_2 \rightarrow S_1$ population transfer at $t = 270\text{ fs}$); (c) time evolution of the electronic states for a prototype trajectory showing $\pi\pi^* \rightarrow \text{gs}$ relaxation ($S_2 \rightarrow S_1$ population transfer at $t = 586\text{ fs}$ and $S_1 \rightarrow S_0$ population transfer at $t = 645\text{ fs}$).

S_1 ($n_O\pi^*$) state until 1 ps. This relaxation mechanism is denoted as $\pi\pi^* \rightarrow n_O\pi^*$ trapping. A typical trajectory leading to the repopulation of the electronic ground state S_0 is depicted in Figure 2c. Here, at $t = 586\text{ fs}$, $S_2 \rightarrow S_1$ population transfer occurs, followed by $S_1 \rightarrow S_0$ transition at $t = 656\text{ fs}$. Subsequent to the initial $S_2 \rightarrow S_1$ hopping event, the $\pi\pi^*$ character of the populated state is preserved, leading to a S_1/S_0 conical intersection with $\pi\pi^*/\text{gs}$ character. Thus, the trajectory follows diabatically the $\pi\pi^*$ character in the excited electronic states. Inspection of the complete set of trajectories shows that all observed ground-state relaxation events (8 out of 44 trajectories) follow this mechanism. Upon $S_2 \rightarrow S_1$ relaxation, the diabatic $\pi\pi^*$ character of the populated state is preserved, followed by relaxation into the S_0 state. The period that the

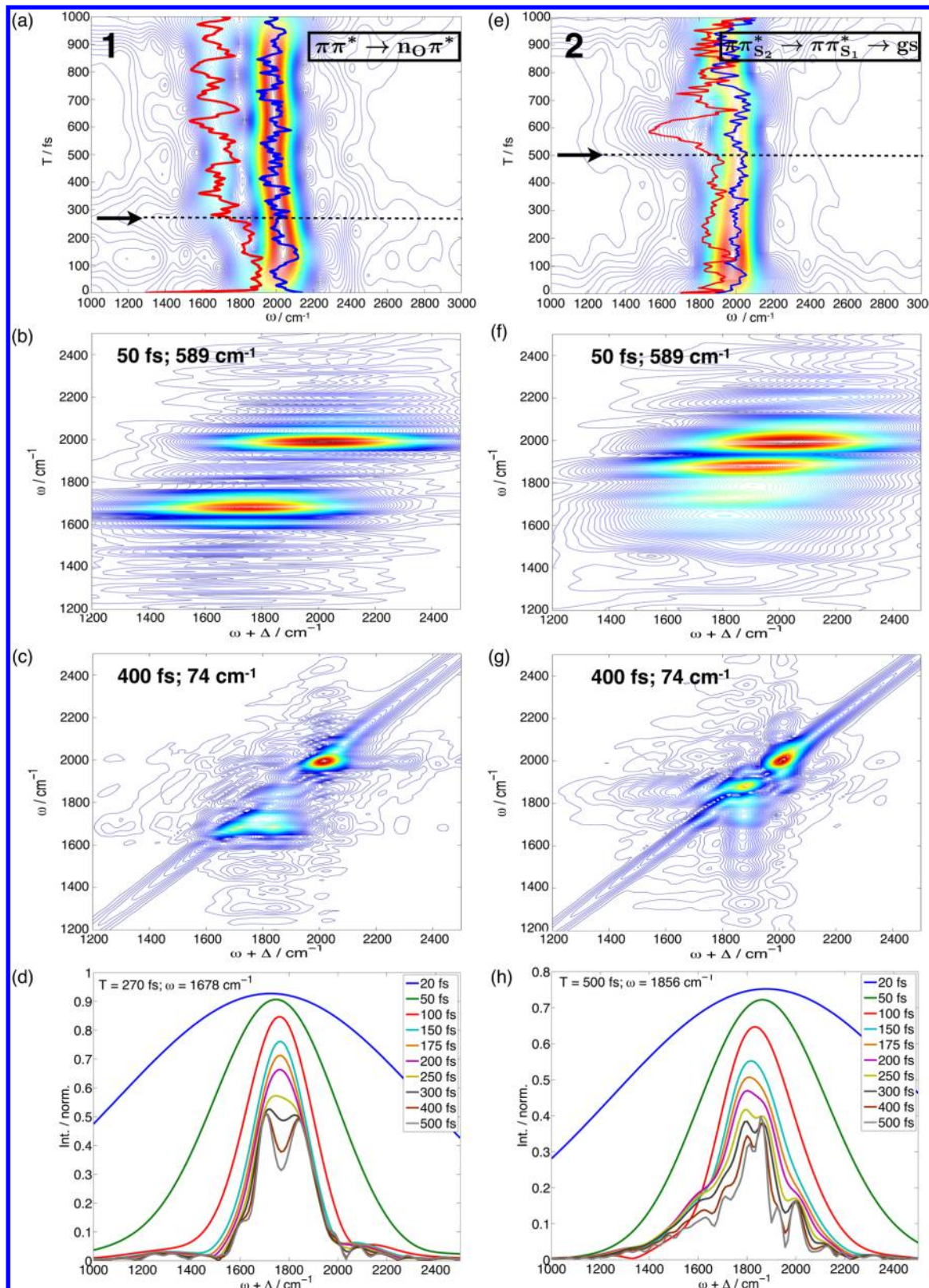


Figure 3. (a) $S_{\text{PP}}(\omega, T)$ signal of the C=O₇ and C=O₈ modes of uracil (Gaussian probe E_2 with $t_{\text{fwhm}} = 175 \text{ fs}$, centered at $\omega_0 = 2000 \text{ cm}^{-1}$; $\Delta T = 25 \text{ fs}$) for the prototype trajectory of $\pi\pi^* \rightarrow n_O\pi^*$ trapping ($S_2 \rightarrow S_1$ population transfer at $t = 270 \text{ fs}$). Also shown are the instantaneous C=O stretch vibrational frequencies. (b) The Δ -dispersed signal $\bar{S}(\omega, T = 270 \text{ fs}; \Delta)$ (5) for a probe pulse characterized by t_{fwhm} and ω_{fwhm} as indicated. (c) Same as (b) but for $t_{\text{fwhm}} = 400 \text{ fs}$ and $\omega_{\text{fwhm}} = 74 \text{ cm}^{-1}$. (d) $\bar{S}(\omega = 1678 \text{ cm}^{-1}, T = 270 \text{ fs}; \Delta)$ for various probe durations. (e–h) Same as (a–d) but for a trajectory of diabatic $\pi\pi_{S_2}^* \rightarrow \pi\pi_{S_1}^* \rightarrow \text{gs}$ relaxation ($S_2 \rightarrow S_1$ population transfer at $t = 586 \text{ fs}$; $S_1 \rightarrow S_0$ population transfer at $t = 645 \text{ fs}$); the Δ -dispersed signal (f–h) is evaluated at $T = 500 \text{ fs}$.

system spends in the intermediate S_1 state varies between 8 and 59 fs, which is too short for a transient increase in the S_1 population.

A possible excited-state relaxation mechanism is summarized in Figure 1b. Subsequent to population of the bright $\pi\pi^*$ state, ultrafast branching of the excited-state population takes place. The dominant relaxation channel involves subpicosecond population transfer involving the $\pi\pi^*$ and $n_O\pi^*$ states, followed by trapping of the population in a dark $n_O\pi^*$ state ($\pi\pi^* \rightarrow n_O\pi^*$ trapping mechanism, right side of Figure 1b); $n_O\pi_{S_1}^* \rightarrow gs$ relaxation could only be observed as a minor channel for propagation times > 1 ps (an elaborate comparison to the relaxation dynamics reported in refs 20 and 21 and electronic populations until $t = 2$ ps are given in the SI). In a parallel relaxation channel, the system relaxes to the S_2 minimum potentially followed by a relaxation into the electronic ground state within the first picosecond. The latter is triggered by a crossing of the $n_O\pi^*$ and $\pi\pi^*$ state, where the diabatic $\pi\pi^*$ character is preserved in the populated S_1 state, followed by $S_1 \rightarrow S_0$ population transfer (diabatic $\pi\pi_{S_2}^* \rightarrow \pi\pi_{S_1}^* \rightarrow gs$ relaxation mechanism; left side of Figure 1b).

UV Pump–IR Probe Signal. In the following, we demonstrate how the two nonadiabatic relaxation mechanisms show up in the temporal evolution of the UV pump–IR probe signal $S_{pp}(\omega, T)$. Figure 3a depicts the $S_{pp}(\omega, T)$ signal (eq 4) of the $\pi\pi^* \rightarrow n_O\pi^*$ trapping (selected time slices are given in SI Figure 6). The calculation is based on a single trajectory and is depicted together with the instantaneous time evolution of the $C=O_7$ and $C=O_8$ stretch vibrations (blue and red lines, respectively). These are modulated due to nonadiabatic electronic relaxation in the bath of all remaining vibrational modes. Both modes $C=O_7$ and $C=O_8$ show fast modulations on a 10–20 fs time scale and slower intense modulations on a 50–100 fs time scale. The $C=O_8$ mode is shifted in its center frequency to $\tilde{\nu} \approx 1700$ cm⁻¹, appearing as new resonance at $t > 270$ fs due to the $\pi\pi^* \rightarrow n_O\pi^*$ population transfer. Detailed comparison of $S_{pp}(\omega, T)$ with the actual time evolution of the $C=O_8$ mode reveals that the new resonance in $S_{pp}(\omega, T)$ slightly precedes $C=O_8$, an intrinsic effect of the path integral expression in eq 4 as the signal does not simply represent an instantaneous snapshot of the vibrational frequency at the observation time (represented by the IR probe pulse centered around T). Due to the population of the S_1 state ($n_O\pi^*$), the relative intensity at $\tilde{\nu} \approx 1700$ cm⁻¹ is reduced compared to the $C=O_7$ mode, but still a clear IR signature of the $\pi\pi^* \rightarrow n_O\pi^*$ trapping process is retained in $S_{pp}(\omega, T)$.

The fast frequency fluctuations apparent in $C=O_7$ and $C=O_8$ are not resolved in the pump–probe signal because the IR probe pulse is too long ($t_{fwhm} = 175$ fs), yet the two modes are resolved. Only frequency shifts that capture the average of the $C=O_{7,8}$ modulations can be observed. To examine the effect of the inherent matter chirp on the joint time–frequency resolution, we decompose the signal in the form

$$S_{pp}(\omega, T) = \mathcal{J} \int_{-\infty}^{\infty} \frac{d\Delta}{2\pi} \mathcal{E}_2^*(\omega) \bar{S}(\omega, T; \Delta) \quad (5)$$

The Δ -dispersed signal $\bar{S}(\omega, T; \Delta)$ (calculated according to SI eq 5) represents the contribution of the $\omega + \Delta$ mode of the probe to the signal (in addition to the ω mode) and is a joint property of field + matter, which depends on the vibrational dynamics as well as the pump and the probe pulses. The signal (eq 4) is obtained by integrating it over Δ . As is clear from eq

S, \bar{S} is not an experimental observable, but it allows one to visualize the underlying paths in the joint field + matter space that contribute to the signal. If the vibrational dynamics is fast compared to the pulse, the signal will depend on the entire probe bandwidth, and the variation of \bar{S} with Δ will resemble the probe envelope. In the opposite limit, only a slice of the bandwidth will participate. In the time domain, this implies that τ_3 in eq 4 will be sharply peaked or diffuse in the two limits, respectively. This will affect the temporal resolution of the technique, as will be demonstrated below.

It is our objective to capture the matter dynamics, that is, the frequency changes of $C=O_{7,8}$ induced by nonadiabatic relaxation in Figure 3a. Therefore, we consider the effect of a 50 fs probe pulse on $\bar{S}(\omega, T; \Delta)$ (Figure 3b). As the probe is short compared to the change in vibrational frequency, $\mathcal{E}_2(\tau_3 - T)$ selects limited frequency contributions from the matter chirp in the time domain. Accordingly, the dominant contribution in $\bar{S}(\omega, T; \Delta)$ arises from the broad bandwidth of the pulse itself, and frequency resolution of matter is eroded (see the two unstructured bands along $\omega + \Delta$ in Figure 3b). For a long 400 fs probe pulse (Figure 3c), the induced frequency changes $C=O_{7,8}$ are entirely captured by the probe field, and we obtain a high-frequency resolution with dominant frequency contributions arising from the matter (at the expense of low temporal resolution). Each resonance along ω can now be decomposed into matter–frequency contributions at a given delay T . Figure 3d displays the underlying frequency contributions to a single point in $S_{pp}(\omega, T)$ for different probe durations. For long pulses (300–500 fs), the induced frequency changes $C=O_{7,8}$ are captured by the probe pulse, resulting in a double peak structure that corresponds to the initial and final frequency of $C=O_8$ due to the nonadiabatic relaxation. The width of \bar{S} along $\omega + \Delta$ becomes independent of the probe due to the inherent matter chirp contribution (for a comparison with the probe bandwidth see SI Figure 5). As the probe is shortened (250–150 fs), $\mathcal{E}_2(\tau_3 - T)$ selects only limited frequency contributions from the matter chirp. Thus, frequency resolution is reduced, and non-Gaussian peak shapes appear along $\omega + \Delta$. In the limit when the probe is short compared to the change in the vibrational frequency $C=O_{7,8}$ (20–50 fs), the dominant contribution to $\bar{S}(\omega, T; \Delta)$ arises from the pulse itself, and frequency resolution is eroded.

A similar analysis for the diabatic $\pi\pi_{S_2}^* \rightarrow \pi\pi_{S_1}^* \rightarrow gs$ relaxation trajectory is shown in Figure 3e–h. In the $S_{pp}(\omega, T)$ signal (Figure 3e), the intensity of the low-energy $C=O_8$ mode is now largely diminished. Only one resonance appears from the $C=O_7$ mode, which shows a characteristic blue shift until $t = 500$ fs due to its evolution on the S_2 potential energy surface with $\pi\pi^*$ character. The nonadiabatic relaxation mediated by a $\pi\pi^* \rightarrow gs$ conical intersection shows up in a short spike in the signal due to dramatic red shift in $C=O_8$, which is already initiated by the $\pi\pi_{S_2}^* \rightarrow \pi\pi_{S_1}^*$ population transfer. Upon relaxation into S_0 , the frequency shift is reversed, and both modes $C=O_7$ and $C=O_8$ again appear at around $\tilde{\nu} = 2000$ cm⁻¹. Further on, $C=O_8$ and $C=O_7$ appear highly oscillating due to excess vibrational energy in S_0 . The individual modes are not resolved; nevertheless, the ground-state relaxation is accompanied by a strong increase in intensity showing up in $S_{pp}(\omega, T)$. By examining the Δ -dispersed signal $\bar{S}(\omega, T = 500$ fs; Δ) we observe that for a long probe pulse, a structured red-shifted shoulder along $\omega + \Delta$ can be observed at $\omega = 1856$ cm⁻¹ (Figure 3g), which arises from the matter-induced

changes in vibrational frequency due to nonadiabatic relaxation. An examination of these frequency contributions as a function of pulse duration (Figure 3h) reveals that probe pulses of 150–250 fs are required to resolve this spectral feature. Interestingly, the system dynamics-induced frequency changes of $C=O_{7/8}$ of both relaxation mechanisms appear on a similar ~ 100 fs time scale, imposing common requirements on the design of probe pulse length and bandwidth. We find that probe pulses of $t_{\text{fwhm}} = 150$ –250 fs offer the best compromise of temporal and spectral resolution, which allows one to resolve spectral features characteristic for the individual relaxation mechanisms (see, e.g., the shoulder at $\omega + \Delta \approx 1500$ –1600 cm^{-1} for $t_{\text{fwhm}} = 200$ fs in Figure 3h).

The signal $S_{\text{pp}}(\omega, T)$ obtained by ensemble averaging $\langle \dots \rangle_e$ over the set of trajectories is depicted in Figure 4a. We observe

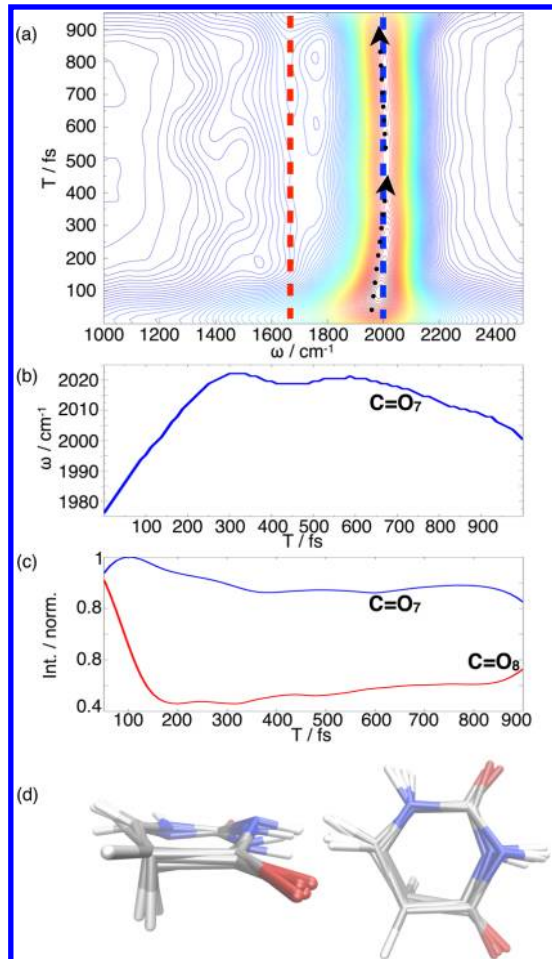


Figure 4. (a) Signal $S_{\text{pp}}(\omega, T)$ of $C=O_7$ and $C=O_8$ modes averaged over 44 trajectories. \mathcal{E}_2 pulse parameters: $t_{\text{fwhm}} = 175$ fs, $\omega_0 = 2000$ cm^{-1} ; $\Delta T = 25$ fs. (b) Peak shift of the $C=O_7$ vibrational frequency as indicated by black dots in (a). (c) Time evolution of the $C=O_7$ and $C=O_8$ vibrational frequency. (d) Overlay of S_1/S_0 CoIn structures reached during the dynamics.

a single intense resonance at around $\tilde{\nu} = 2000$ cm^{-1} originating from the time evolution of the $C=O_7$ mode. The frequency and its intensity evolution are depicted in Figure 4b and c, respectively (blue line). By analyzing the spectral position of the $C=O_7$ mode (Figure 4b), we observe an initial blue shift of the center frequency until $t = 300$ fs due to the initial dynamics in the S_2 and S_1 states, followed by a red shift of $\Delta\tilde{\nu} = 20$ cm^{-1}

for $t > 600$ fs. The intensity of the $C=O_7$ mode is initially diminished until 400–500 fs by about 15% (Figure 4c). Later on, we observe a recovery in the spectral region at around $\tilde{\nu} = 2000$ cm^{-1} due to population of the electronic ground state. Both the temporal intensity recovery and red shift of the center frequency are clear spectroscopic signatures of the diabatic $\pi\pi_{S_2}^* \rightarrow \pi\pi_{S_1}^*$ transition, which is responsible for the ultrafast photoprotection mechanism of uracil. In the course of the dynamics, ground-state relaxation is mediated by the superimposed S_1/S_0 CoIn structures depicted in Figure 4d, representing the active part of the $\pi\pi_{S_1}^* \rightarrow \text{gs}$ CoIn seam. They are characterized by a pronounced pyramidalization at C5 accompanied by an out-of-plane displacement of HS, in good agreement with the lowest-energy S_1/S_0 CoIn characterized in refs 16, 19, and 50. Additionally, the dynamically reached CoIn structures show an out-of-plane displacement of N3 and C6, where the degree of C5 pyramidalization can be compensated for by an N3 and C6 Dewar-like structure.^{34,51}

The spectral signature of the $\pi\pi^* \rightarrow n_O\pi^*$ trapping appears red-shifted to the intense $C=O_7$ mode in the ensemble-averaged signal $S_{\text{pp}}(\omega, T)$ as a broad and unstructured plateau with about 15% intensity compared to the intense $C=O_7$ mode. The plateau-like appearance arises from the excess vibrational energy in the $n_O\pi^*$ state populated by nonadiabatic relaxation. The plateau intensity steadily increases from $t > 300$ fs (red line in Figure 4c), providing a unique signature of the dynamics of the optical dark $n_O\pi^*$ state. Similar red-shifted features have been reported for thymine and thymidine but on a slower nanosecond time scale, indicative of triplet-state formation.⁵² As both the $C=O_8$ carbonyl bonds of a ${}^1n_O\pi^*$ and a ${}^3\pi\pi^*$ state possess substantial single-bond character, similar signatures on the respective (femtosecond or nanosecond) time scales are expected.

We have reported simulations of the time-resolved UV pump–IR probe signal $S_{\text{pp}}(\omega, T)$ of the RNA nucleobase uracil undergoing nonadiabatic electronic relaxation. The pump–probe signal should help to unambiguously reveal the interconnected relaxation pathways in future time-resolved measurements. We find that both diabatic $\pi\pi_{S_2}^* \rightarrow \pi\pi_{S_1}^*$ → gs relaxation and $\pi\pi^* \rightarrow n_O\pi^*$ trapping mechanisms have distinct signatures within the first picosecond in $S_{\text{pp}}(\omega, T)$. The system dynamics time scale imposes a lower bound on the probe pulse and defines the actual time resolution that can be observed in the experiment. There are two fundamental reasons why the signal (eq 4) may not be interpreted as snapshots of the instantaneous vibrational frequency, (1) the uncertainty in τ_3 around T limits our ability to initiate the probe process in a sharply defined time, and (2) the signal at time T depends on a time integral over the frequency trajectory rather than its value at one time. Both effects preclude the simple interpretation of the signal by inspection. However, using modeling, the molecular relaxation parameters may nevertheless be extracted from the signals. Some information of the individual trajectories (i.e., individual nonadiabatic relaxation events) is missed in the ensemble-averaged spectra. Performing nonlinear optical experiments at the single-molecule level where individual trajectories can be observed will be an exciting possibility.^{53–55}

THEORETICAL METHODS

The signal is calculated in the semiclassical signal representation (eq 4) where all required molecular quantities are derived

from semiclassical nonadiabatic on-the-fly molecular molecular dynamics trajectory calculations. We follow a three step procedure.

(1) Nonadiabatic On-the-Fly Molecular Dynamics (NA-O-MD). NA-O-MD simulations are performed with the *Newton-X* program package⁵⁶ where the nuclei are treated classically and follow Newton's equation of motion. The acceleration on the nuclei is defined by the gradient $\partial E^S(R)/\partial R$ of the respective populated electronic state i . Excited-state gradients are evaluated by solving the time-independent Schrödinger equation for the electrons and a subsequent gradient calculation based on the Ehrenfest theorem.^{57,58} For the integration of the electronic Hamiltonian, the electronic expansion coefficients c_{kj} define the time-dependent electronic population, where changes are induced by the quantum chemically derived coupling vector $d_{kj}(R)$, the velocity vector \dot{R} (defined by the PES gradient), and the potential energy matrix V_{kj} , which is diagonal in the adiabatic representation. Computational details of the NA-O-MD simulations are given in the SI.

(2) Reconstruction of the Excited-State Vibrational Hamiltonian. The NA-O-MD simulations yield trajectories of the electronic state potential energies $E_i(t)$ together with the evolving nuclear geometries $q(t)$ as classical objects. We follow the intramolecular high-frequency spectator modes (i.e., the C=O vibrations) whose frequencies are modulated during the dynamics in the bath of all other nuclear motions in the style of instantaneous normal-mode analysis^{59–62} where the spectator modes possess stable (real) eigenvalues during the dynamics. For low-frequency skeleton motions, the semiclassical signal representation loses validity as the modes can potentially evolve from stable to unstable (and vice versa). Here, a full quantum propagation of the Green's function according to eqs 2 and 3 is required. The standard approach for the calculation of vibrational frequencies is the diagonalization of the full (mass-weighted) Hessian matrix (within the harmonic approximation), yielding $3N - 6$ vibrational eigenvalues and eigenvectors at time t . To follow the excited-state dynamics of the C=O vibrations of nucleobases, a block diagonal Hessian can be constructed in an iterative subspace Davidson procedure,⁴² avoiding the calculation of the full excited-state Hessian. This mode tracking procedure allows one to follow the important modes in the spectrum, which are known a priori without the need to calculate the full Hessian matrix. Thus, omitting unnecessary modes, the numerical effort is decoupled from the system size. The computational details of the mode tracking procedure are given in the SI.

(3) IR Intensities. We approximate the IR intensities by neglecting the nuclear coordinate dependence but taking into account the relative intensity of vibrational modes in the different electronic excited states (Franck–Condon approximation). Non-Codon effects can be incorporated by numerical differentiation of the excited-state dipole moment with respect to the ‘fingerprint’ normal modes q_i .

■ ASSOCIATED CONTENT

Supporting Information

Computational details of the nonadiabatic on-the-fly molecular dynamics and mode tracking procedure. Expressions for the Δ -dispersed signal $\bar{S}(\omega, T; \Delta)$. Discussion of the time evolution of the electronic states and populations. Supporting figures of the Δ -dispersed signal $\bar{S}(\omega, T; \Delta)$. This material is available free of charge via the Internet at <http://pubs.acs.org>.

■ AUTHOR INFORMATION

Corresponding Author

*E-mail: smukamel@uci.edu; bfingerh@uci.edu; dorfman@gmail.com.

Notes

The authors declare no competing financial interest.

■ ACKNOWLEDGMENTS

We gratefully acknowledge the support of the National Institute of Health Grant No. GM-59230, National Science Foundation through Grant No. CHE-1058791, the Chemical Sciences, Geosciences and Biosciences Division, Office of Basic Energy Sciences, Office of Science and U.S. Department of Energy. B.P.F. gratefully acknowledges support from the Alexander-von-Humboldt Foundation through the Feodor-Lynen program. We would like to thank the Leibniz-Rechenzentrum and the Greenplanet cluster (Grant No. CHE-0840513) for the allocation of computing resources.

■ REFERENCES

- Crespo-Hernández, C. E.; Cohen, B.; Hare, P. M.; Kohler, B. Ultrafast Excited-State Dynamics in Nucleic Acids. *Chem. Rev.* **2004**, *104*, 1977–2020.
- Middleton, C. T.; de La Harpe, K.; Su, C.; Law, Y. K.; Crespo-Hernández, C. E.; Kohler, B. DNA Excited-State Dynamics: From Single Bases to the Double Helix. *Annu. Rev. Phys. Chem.* **2009**, *60*, 217–239.
- Schreier, W. J.; Schrader, T. E.; Koller, F. O.; Gilch, P.; Crespo-Hernández, C. E.; Swaminathan, V. N.; Carell, T.; Zinth, W.; Kohler, B. Thymine Dimerization in DNA is an Ultrafast Photoreaction. *Science* **2007**, *315*, 625–629.
- Schreier, W. J.; Kubon, J.; Regner, N.; Haiser, K.; Schrader, T. E.; Zinth, W.; Clivio, P.; Gilch, P. Thymine Dimerization in DNA Model Systems: Cyclobutane Photolesion is Predominantly Formed via the Singlet Channel. *J. Am. Chem. Soc.* **2009**, *131*, 5038–5039.
- Crespo-Hernández, C. E.; Cohen, B.; Kohler, B. Base Stacking Controls Excited-State Dynamics in A-T DNA. *Nature* **2005**, *436*, 1141–1144.
- Markovitsi, D.; Talbot, F.; Gustavsson, T.; Onidas, D.; Lazzarotto, E.; Marguet, S. Molecular Spectroscopy: Complexity of Excited-State Dynamics in DNA. *Nature* **2006**, *441*, E7; discussion E8.
- Vayá, I.; Gustavsson, T.; Miannay, F.-A.; Douki, T.; Markovitsi, D. Fluorescence of Natural DNA: From the Femtosecond to the Nanosecond Time Scales. *J. Am. Chem. Soc.* **2010**, *132*, 11834–11835.
- Ullrich, S.; Schultz, T.; Zgierski, M. Z.; Stolow, A. Electronic Relaxation Dynamics in DNA and RNA Bases Studied by Time-Resolved Photoelectron Spectroscopy. *Phys. Chem. Chem. Phys.* **2004**, *6*, 2796–2801.
- Canuel, C.; Mons, M.; Piuzzi, F.; Tardivel, B.; Dimicoli, I.; Elhanine, M. Excited States Dynamics of DNA and RNA Bases: Characterization of a Stepwise Deactivation Pathway in the Gas Phase. *J. Chem. Phys.* **2005**, *122*, 074316.
- Satzger, H.; Townsend, D.; Zgierski, M. Z.; Patchkovskii, S.; Ullrich, S.; Stolow, A. Primary Processes Underlying the Photostability of Isolated DNA Bases: Adenine. *Proc. Natl. Acad. Sci. U.S.A.* **2006**, *103*, 10196–10201.
- Perun, S.; Sobolewski, A.; Domcke, W. Ab Initio Studies on the Radiationless Decay Mechanisms of the Lowest Excited Singlet States of 9H-Adenine. *J. Am. Chem. Soc.* **2005**, *127*, 6257–6265.
- Sobolewski, A. L.; Domcke, W.; Dedonder-Lardeux, C.; Jouvet, C. Excited-State Hydrogen Detachment and Hydrogen Transfer Driven by Repulsive $1\pi\sigma^*$ States: A New Paradigm for Nonradiative Decay in Aromatic Biomolecules. *Phys. Chem. Chem. Phys.* **2002**, *4*, 1093–1100.

- (13) Yamazaki, S.; Domcke, W.; Sobolewski, A. L. Nonradiative Decay Mechanisms of the Biologically Relevant Tautomer of Guanine. *J. Phys. Chem. A* **2008**, *112*, 11965–11968.
- (14) Barbatti, M.; Aquino, A. J. A.; Szymczak, J. J.; Nachtigallová, D.; Hobza, P.; Lischka, H. Relaxation Mechanisms of UV-Photoexcited DNA and RNA Nucleobases. *Proc. Natl. Acad. Sci. U.S.A.* **2010**, *107*, 21453–21458.
- (15) Ismail, N.; Blancafort, L.; Olivucci, M.; Kohler, B.; Robb, M. A. Ultrafast Decay of Electronically Excited Singlet Cytosine via a $\pi\pi^*$ to $n_0\pi^*$ State Switch. *J. Am. Chem. Soc.* **2002**, *124*, 6818–6819.
- (16) Matsika, S. Radiationless Decay of Excited States of Uracil through Conical Intersections. *J. Phys. Chem. A* **2004**, *108*, 7584–7590.
- (17) Asturiol, D.; Lasorne, B.; Robb, M. A.; Blancafort, L. Photophysics of the $\pi\pi^*$ and n,π^* States of Thymine: MS-CASPT2 minimum-Energy Paths and CASSCF On-the-Fly Dynamics. *J. Phys. Chem. A* **2009**, *113*, 10211–10218.
- (18) Gustavsson, T.; Bányász, A.; Lazzarotto, E.; Markovitsi, D.; Scalmani, G.; Frisch, M. J.; Barone, V.; Improta, R. Singlet Excited-State Behavior of Uracil and Thymine in Aqueous Solution: A Combined Experimental and Computational Study of 11 Uracil Derivatives. *J. Am. Chem. Soc.* **2006**, *128*, 607–619.
- (19) Hare, P. M.; Crespo-Hernández, C. E.; Kohler, B. Internal Conversion to the Electronic Ground State Occurs via Two Distinct Pathways for Pyrimidine Bases in Aqueous Solution. *Proc. Natl. Acad. Sci. U.S.A.* **2007**, *104*, 435–440.
- (20) Hudock, H. R.; Levine, B. G.; Thompson, A. L.; Satzger, H.; Townsend, D.; Gador, N.; Stolow, A.; Martinez, T. J. Ab Initio Molecular Dynamics and Time-Resolved Photoelectron Spectroscopy of Electronically Excited Uracil and Thymine. *J. Phys. Chem. A* **2007**, *111*, 8500–8508.
- (21) Nachtigallová, D.; Aquino, A. J. A.; Szymczak, J. J.; Barbatti, M.; Hobza, P.; Lischka, H. Nonadiabatic Dynamics of Uracil: Population Split among Different Decay Mechanisms. *J. Phys. Chem. A* **2011**, *115*, 5247–5255.
- (22) Lan, Z.; Fabiano, E.; Thiel, W. Photoinduced Nonadiabatic Dynamics of Pyrimidine Nucleobases: On-the-Fly Surface-Hopping Study with Semiempirical Methods. *J. Phys. Chem. B* **2009**, *113*, 3548–3555.
- (23) Selig, U.; Schleussner, C.-F.; Foerster, M.; Langhofer, F.; Nuernberger, P.; Brixner, T. Coherent Two-Dimensional Ultraviolet Spectroscopy in Fully Noncollinear Geometry. *Opt. Lett.* **2010**, *35*, 4178–4180.
- (24) Tseng, C.-H.; Sándor, P.; Kotur, M.; Weinacht, T. C.; Matsika, S. Two-Dimensional Fourier Transform Spectroscopy of Adenine and Uracil Using Shaped Ultrafast Laser Pulses in the Deep UV. *J. Phys. Chem. A* **2012**, *116*, 2654–2661.
- (25) West, B. A.; Moran, A. M. Two-Dimensional Electronic Spectroscopy in the Ultraviolet Wavelength Range. *J. Phys. Chem. Lett.* **2012**, *3*, 2575–2581.
- (26) Krebs, N.; Pugliesi, I.; Riedle, E. Pulse Compression of Ultrashort UV Pulses by Self-Phase Modulation in Bulk Material. *Appl. Sci.* **2013**, *3*, 153–167.
- (27) Widom, J. R.; Johnson, N. P.; von Hippel, P. H.; Marcus, A. H. Solution Conformation of 2-Aminopurine Dinucleotide Determined by Ultraviolet Two-Dimensional Fluorescence Spectroscopy. *New J. Phys.* **2013**, *15*, 025028.
- (28) West, B. A.; Giokas, P. G.; Molesky, B. P.; Ross, A. D.; Moran, A. M. Toward Two-Dimensional Photon Echo Spectroscopy with 200 nm Laser Pulses. *Opt. Express* **2013**, *21*, 2118–2125.
- (29) Anfinrud, P. A.; Han, C.; Hochstrasser, R. M. Direct Observations of Ligand Dynamics in Hemoglobin by Subpicosecond Infrared Spectroscopy. *Proc. Natl. Acad. Sci. U.S.A.* **1989**, *86*, 8387–8391.
- (30) Heyne, K.; Mohammed, O.; Usman, A.; Dreyer, J.; Nibbering, E.; Cusanovich, M. Structural Evolution of the Chromophore in the Primary Stages of Trans/Cis Isomerization in Photoactive Yellow Protein. *J. Am. Chem. Soc.* **2005**, *127*, 18100–18106.
- (31) Mohammed, O. F.; Pines, D.; Dreyer, J.; Pines, E.; Nibbering, E. T. J. Sequential Proton Transfer through Water Bridges in Acid–Base Reactions. *Science* **2005**, *310*, 83–86.
- (32) Lim, M.; Jackson, T. A.; Anfinrud, P. A. Binding of CO to Myoglobin from a Heme Pocket Docking Site to Form Nearly Linear Fe–C–O. *Science* **1995**, *269*, 962–966.
- (33) Adamczyk, K.; Prémont-Schwarz, M.; Pines, D.; Pines, E.; Nibbering, E. T. J. Real-Time Observation of Carbonic Acid Formation in Aqueous Solution. *Science* **2009**, *326*, 1690–1694.
- (34) Haiser, K.; Fingerhut, B. P.; Heil, K.; Glas, A.; Herzog, T. T.; Pilles, B. M.; Schreier, W. J.; Zinth, W.; de Vivie-Riedle, R.; Carell, T. Mechanism of UV-Induced Formation of Dewar Lesions in DNA. *Angew. Chem., Int. Ed.* **2012**, *51*, 408–411.
- (35) Fingerhut, B. P.; Herzog, T. T.; Ryseck, G.; Haiser, K.; Graupner, F. F.; Heil, K.; Gilch, P.; Schreier, W. J.; Carell, T.; de Vivie-Riedle, R.; Zinth, W. Dynamics of Ultraviolet-Induced DNA Lesions: Dewar Formation Guided by Pre-Tension Induced by the Backbone. *New J. Phys.* **2012**, *14*, 065006.
- (36) Mohammed, O. F.; Adamczyk, K.; Banerji, N.; Dreyer, J.; Lang, B.; Nibbering, E. T. J.; Vauthay, E. Direct Femtosecond Observation of Tight and Loose Ion Pairs upon Photoinduced Bimolecular Electron Transfer. *Angew. Chem., Int. Ed.* **2008**, *47*, 9044–9048.
- (37) Kukura, P.; McCamant, D. W.; Mathies, R. A. Femtosecond Stimulated Raman Spectroscopy. *Annu. Rev. Phys. Chem.* **2007**, *58*, 461–488.
- (38) Umapathy, S.; Lakshmanna, A.; Mallick, B. Ultrafast Raman Loss Spectroscopy. *J. Raman Spectrosc.* **2009**, *40*, 235–237.
- (39) Kuramochi, H.; Takeuchi, S.; Tahara, T. Ultrafast Structural Evolution of Photoactive Yellow Protein Chromophore Revealed by Ultraviolet Resonance Femtosecond Stimulated Raman Spectroscopy. *J. Phys. Chem. Lett.* **2012**, *3*, 2025–2029.
- (40) Mukamel, S.; Biggs, J. D. Communication: Comment on the Effective Temporal and Spectral Resolution of Impulsive Stimulated Raman Signals. *J. Chem. Phys.* **2011**, *134*, 161101.
- (41) Dorfman, K. E.; Fingerhut, B. P.; Mukamel, S. Broadband Infrared and Raman Probes of Excited-State Vibrational Molecular Dynamics; Simulation Protocols Based on Loop Diagrams. *Phys. Chem. Chem. Phys.* **2013**, accepted; DOI: <http://arxiv.org/abs/1305.5291>.
- (42) Reiher, M.; Neugebauer, J. A Mode-Selective Quantum Chemical Method for Tracking Molecular Vibrations Applied to Functionalized Carbon Nanotubes. *J. Chem. Phys.* **2003**, *118*, 1634–1641.
- (43) Rahav, S.; Mukamel, S. Ultrafast Nonlinear Optical Signals Viewed from the Molecules Perspective: Kramers–Heisenberg Transition Amplitudes vs. Susceptibilities. *Adv. At., Mol., Opt. Phys.* **2010**, *59*, 223–263.
- (44) Cheng, J.-X.; Volkmer, A.; Book, L. D.; Xie, X. S. Multiplex Coherent Anti-Stokes Raman Scattering Microspectroscopy and Study of Lipid Vesicles. *J. Phys. Chem. B* **2002**, *106*, 8493–8498.
- (45) Müller, M.; Schins, J. M. Imaging the Thermodynamic State of Lipid Membranes with Multiplex CARS Microscopy. *J. Phys. Chem. B* **2002**, *106*, 3715–3723.
- (46) Kee, T. W.; Cicerone, M. T. Simple Approach to One-Laser, Broadband Coherent Anti-Stokes Raman Scattering Microscopy. *Opt. Lett.* **2004**, *29*, 2701–2703.
- (47) Volkmer, A. Vibrational Imaging and Microspectroscopies Based on Coherent Anti-Stokes Raman Scattering Microscopy. *J. Phys. D: Appl. Phys.* **2005**, *38*, R59–R81.
- (48) von Vacano, B.; Meyer, L.; Motzkus, M. Rapid Polymer Blend Imaging with Quantitative Broadband Multiplex CARS Microscopy. *J. Raman Spectrosc.* **2007**, *38*, 916–926.
- (49) Harsányi, L.; Császár, P.; Császár, A.; Boggs, J. E. Interpretation of the Vibrational Spectra of Matrix-Isolated Uracil from Scaled Ab Initio Quantum Mechanical Force Fields. *Int. J. Quantum Chem.* **1986**, *29*, 799–815.
- (50) Delchev, V. B.; Sobolewski, A.; Domcke, W. Comparison of the Non-Radiative Decay Mechanisms of 4-Pyrimidinone and Uracil: An Ab Initio Study. *Phys. Chem. Chem. Phys.* **2010**, *12*, 5007–5015.

- (51) Fingerhut, B. P.; Oesterling, S.; Haiser, K.; Heil, K.; Glas, A.; Schreier, W. J.; Zinth, W.; Carell, T.; de Vivie-Riedle, R. ONIOM Approach for Non-Adiabatic On-the-Fly Molecular Dynamics Demonstrated for the Backbone Controlled Dewar Valence Isomerization. *J. Chem. Phys.* **2012**, *136*, 204307.
- (52) Hare, P. M.; Middleton, C. T.; Mertel, K. I.; Herbert, J. M.; Kohler, B. Time-Resolved Infrared Spectroscopy of the Lowest Triplet State of Thymine and Thymidine. *Chem. Phys.* **2008**, *347*, 383–392.
- (53) Chong, S.; Min, W.; Xie, X. S. Ground-State Depletion Microscopy: Detection Sensitivity of Single-Molecule Optical Absorption at Room Temperature. *J. Phys. Chem. Lett.* **2010**, *1*, 3316–3322.
- (54) Jung, Y.; Slipchenko, M. N.; Liu, C. H.; Ribbe, A. E.; Zhong, Z.; Yang, C.; Cheng, J.-X. Fast Detection of the Metallic State of Individual Single-Walled Carbon Nanotubes Using a Transient-Absorption Optical Microscope. *Phys. Rev. Lett.* **2010**, *105*, 217401.
- (55) Sheps, T.; Brocious, J.; Corso, B. L.; Güll, O. T.; Whitmore, D.; Durkaya, G.; Potma, E. O.; Collins, P. G. Four-Wave Mixing Microscopy with Electronic Contrast of Individual Carbon Nanotubes. *Phys. Rev. B* **2012**, *86*, 235412.
- (56) Barbatti, M.; Granucci, G.; Persico, M.; Ruckenbauer, M.; Vazdar, M.; Eckert-Maksic, M.; Lischka, H. The On-the-Fly Surface-Hopping Program System Newton-X: Application to Ab Initio Simulation of the Nonadiabatic Photodynamics of Benchmark Systems. *J. Photochem. Photobiol. A* **2007**, *190*, 228–240.
- (57) Warshel, A. Bicycle-Pedal Model for the First Step in the Vision Process. *Nature* **1976**, *260*, 679–683.
- (58) Tully, J. C. Molecular Dynamics with Electronic Transitions. *J. Chem. Phys.* **1990**, *93*, 1061–1071.
- (59) Buchner, M.; Ladanyi, B. M.; Stratt, R. M. The Short-Time Dynamics of Molecular Liquids. Instantaneous-Normal-Mode Theory. *J. Chem. Phys.* **1992**, *97*, 8522–8535.
- (60) Moore, P.; Keyes, T. Normal Mode Analysis of Liquid CS₂: Velocity Correlation Functions and Self-Diffusion Constants. *J. Chem. Phys.* **1994**, *100*, 6709–6717.
- (61) Nguyen, P. H.; Stock, G. Nonequilibrium Molecular-Dynamics Study of the Vibrational Energy Relaxation of Peptides in Water. *J. Chem. Phys.* **2003**, *119*, 11350–11358.
- (62) Bastida, A.; Soler, M. A.; Zuniga, J.; Requena, A.; Kalstein, A.; Fernandez-Alberti, S. Instantaneous Normal Modes, Resonances, and Decay Channels in the Vibrational Relaxation of the Amide I Mode of N-Methylacetamide-D in Liquid Deuterated Water. *J. Chem. Phys.* **2010**, *132*, 224501.

Supporting Information:

Monitoring Non-Adiabatic Dynamics of the RNA

Base Uracil by UV-Pump-IR-Probe Spectroscopy

Benjamin P. Fingerhut, Konstantin E. Dorfman, and Shaul Mukamel*

Chemistry Department, University of California, Irvine, California 92697-2025, USA

E-mail: smukamel@uci.edu

*To whom correspondence should be addressed

1 Computational Details:

1.1 Computational Details - Non-Adiabatic On-the-fly Molecular Dynamics

(NA-O-MD):

The NA-O-MD simulations of the RNA base uracil rely on the *Newton-X* program package¹, where surface hopping between different electronic states is described by Tully's surface hopping algorithm². The electronic structure calculations to obtain excitation energies, excited state gradients and derivative coupling vectors, are evaluated with the MOLPRO program package (version 2006.1)^{3,4}. The equations of motions of the nuclei are integrated with the Velocity-Verlet algorithm⁵ using a timestep $\Delta t = 0.5$ fs, within this interval a reduced timestep of $\Delta t/20$ is used to interpolate the energy gradients and derivative coupling vectors for a continuous update of the electronic population^{1,6}. For the integration of the electronic Schrödinger equation the unitary propagator is used to account for time-reversal symmetry around the loop, which is not guaranteed for the 5th. order Butcher algorithm⁷. During the dynamics of the individual trajectories the derivative coupling vectors are evaluated between neighboring electronic states, the phase of the derivative coupling vector is followed to avoid phase jumps during the dynamics. The energy conservation of the trajectories is ensured in the following way: first an energy-jump parameter (= 1.0 eV, ≈ 0.01 % of total energy) is used to detect convergence problems especially in solving the CP-MCSCF equations for gradients and non-adiabatic couplings as well as, to a minor extend, of the electronic wavefunction. Second the total energy drift over the propagation time of trajectories is checked manually and to be 0.07 eV (3 % of zero-point vibrational energy) on average for the 44 investigated trajectories determined by the timestep in the Velocity-Verlet algorithm. Similar values have been reported in Ref.⁸. After a hopping event between electronic states, the momentum of the nuclei is adjusted along the direction of the derivative coupling vectors to conserve the total energy. To investigate the femtosecond relaxation dynamics of the RNA base uracil an uncorrelated Wigner distribution of the electronic ground state was sampled and 44 trajectories were used in NA-O-MD simulations for the calculation of the average electronic population and

the UV-Pump - IR-Probe signal $S_{FSIR}(\omega, T)$. As a δ pulse is assumed for the UV photoexcitation all trajectories are chosen without imposing further restrictions on excitation energies. If only a certain frequency window is accessible due to the finite width of the excitation pulse the procedure described in Ref.⁹ can be applied.

In all NA-O-MD simulations the electronic structure of the RNA base uracil is treated on CASSCF level of theory. All π orbitals as well as the two lone pairs (n_{O_7} , n_{O_8}) are included in the active space. The resulting CAS(14/10) wavefunction (CAS(m/n) with m being the number of active electrons and n being the number of active orbitals) allows for a description of all relevant electronic states, namely the electronic ground state (S_0), the optical accessible $\pi\pi^*$ state and two dark states, which correspond to excitations from the n_{O_7} - and n_{O_8} - lone pairs into anti-bonding π^* orbitals ($n_{O_7}\pi^*$, $n_{O_8}\pi^*$). The simulations start in the optical bright $\pi\pi^*$ state (depending on the initial condition either S_2 or S_3) and include the four electronic states S_0 , S_1 ($\pi\pi^*$), S_2 ($n_O\pi^*$) and S_3 ($n_O\pi^*$) during the dynamics, resulting in a *state average* (=sa)-CASSCF wavefunction without symmetry restrictions with four equally weighted states (sa4-CAS(14/10)).

The CASSCF method used for the dynamic simulations leads to an overshooting of the $\pi\pi^*$ state in the Franck-Condon (FC) region (see SI- Table 1) requiring to consider dynamic electron correlation for accurate excitation energies. Nevertheless the characteristics of the excited state potential energy surfaces (like minima, conical intersection and reaction pathways) are reasonably described, as has been investigated in extensive benchmark calculations on uracil on MRCI⁹ and MRPT2¹⁰ level of theory. Interestingly the barriers to reach the conical intersection on the excited state potential energy surface are well described on CASSCF level of theory, allowing to reproduce experimental time constants^{9,11} without a significant speed up of the reaction dynamics on CASSCF level of theory. For all dynamic calculations the 6-31G* basis set is used.

1.2 Computational Details - Reconstruction of the excited state vibrational Hamiltonian (Mode Tracking):

The NA-O-MD simulations yield trajectories of the electronic state potential energies $E_i(t)$ together with the evolving nuclear geometries $q(t)$ as classical objects. The $C = O$ vibrations are evaluated with a time step $\delta t = 2$ fs over the course of the trajectories by the mode tracking algorithm (for details see below). Thus the normal modes are evaluated, depending on the evolution of the trajectory, over the complete normal mode coordinate of the $C = O$ vibrations, i.e. the inner turning point, the equilibrium structure and the outer turning point. This yields a highly oscillating function $\omega(q(t))$ which still contains the dependence on the position of the normal mode coordinate (see dashed lines in Figure 1). In order to obtain the vibrational frequencies $\omega(t)$ of $C = O$ modes during the non-adiabatic dynamics we exploit the fact that fast oscillation occurs around the arithmetic mean, i.e. the equilibrium structure q_0 of the normal mode where the latter evolves in time due to non-adiabatic relaxation. To derive the vibrational frequency around the equilibrium q_0 a linear filter with a filtering window $[t - \Delta W/2; t + \Delta W/2]$ is applied to $\omega(q(t))$. The width of the filtering window $\Delta W = 36$ fs corresponding to ≈ 2 vibrational periods of the $C = O$ modes (see solid lines in Figure 1).

By calculating $C = O$ vibrations over the course of the trajectories we adopt an instantaneous normal mode (INM) approach^{12,13} which was extensively used to study low frequency intermolecular vibrations in liquids to intramolecular high-frequency spectator modes^{14–16} (i.e. the C=O motions). In INM the Hessian matrix, i.e. the matrix of second derivatives of the energy with respect to nuclear coordinates is evaluated at non-equilibrium configurations and the resulting frequencies are partitioned according to stable (real) eigenvalues and unstable (imaginary) eigenvalues. Here the high-frequency spectator modes are modulated during the dynamics in the bath of all other nuclear motions and posses stable (real) eigenvalue due to their spectator character along the reaction coordinate (compare the conical intersection structures in Fig. 4 (d) of the main text). Application to low frequency skeleton motions can be questionable as they can potentially evolve from stable to unstable modes (and *vice versa*). A full quantum propagation of the Green's function according

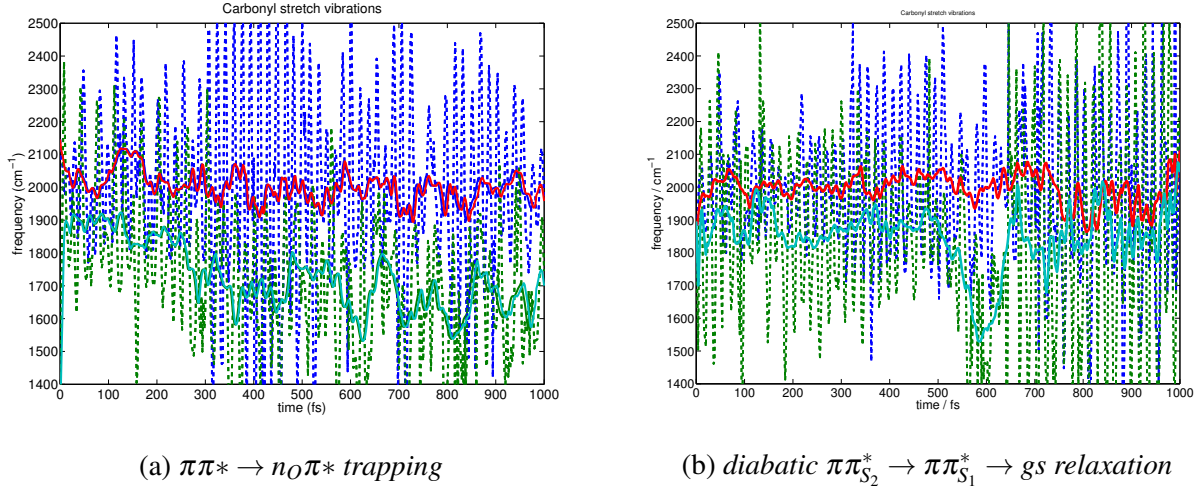


Figure 1: Time-evolution of C=O stretch vibrational frequencies of typical trajectories: The calculated time evolution (partly) contains the self oscillation of the modes and is shown together with a moving average (obtained by applying a linear filter, for details see text) which constitutes the time evolution of the $C = O$ stretch vibrations $\omega_{C=O_8}(t)$ and $\omega_{C=O_7}(t)$ used in the simulation of $S_{PP}(\omega, T)$ (cyan and red lines, respectively). (a) $S_2 \rightarrow S_1$ population transfer occurs at $t = 270$ fs; (b) $S_2 \rightarrow S_1$ population transfer occurs at $t = 586$ fs; $S_1 \rightarrow S_0$ population transfer at $t = 645$ fs

to eq. 2 and 3 of the main text will then be required.

Mode Tracking The standard INM approach is the diagonalization of the full (mass-weighted) Hessian matrix (within the harmonic approximation) at every time step yielding $3N$ eigenvalues and eigenvectors for a molecule containing N atoms

$$(\mathbf{H}^{(m)} - \lambda_i) \mathbf{L}_i = 0, \quad (1)$$

with $\lambda_i \propto \omega_i^2$ being the eigenvalues of the i th vibrational frequency. To follow the excited state dynamics of specific "fingerprint" modes (e.g. the $C = O$ vibrations of DNA nucleobases^{17–20}) a block-diagonal Hessian can be constructed in an iterative subspace Davidson procedure²¹, avoiding the calculation of the full excited state Hessian. In brief, in the mode tracking algorithm the solution of Eq. (1) is avoided and formally replaced by

$$(\mathbf{H}^{(m)} - \lambda_i^{(k)}) \mathbf{L}_i^{(k)} = \mathbf{r}_i^{(k)}, \quad (2)$$

where $\mathbf{r}_i^{(k)}$ is the residuum vector in iteration k for the approximate eigenvector $\mathbf{L}_i^{(k)}$. The numerical procedure starts with a collective displacement \mathbf{b}_i of all atoms for each considered normal mode. The first basis vector serves as an initial guess. In consecutive iterations the normal mode eigenvectors are expanded by the generation of new basis vectors out of the residuum until convergence. By calculating the numerical derivative of the gradient of the electronic energy with respect to the basis vector \mathbf{b} the vectors σ_i are determined by

$$\sigma_i = \mathbf{H}^{(m)} \mathbf{b}_i \quad (3)$$

and used to generate the small Davidson matrix $\tilde{\mathbf{H}}$ with elements

$$\tilde{H}_{ji} = \mathbf{b}_j^T \mathbf{H}^{(m)} \mathbf{b}_i = \mathbf{b}_j^T \sigma_i. \quad (4)$$

The diagonalization of $\mathbf{H}^{(m)}$ yields the approximate eigenvectors $\mathbf{L}_i^{(k)}$ and eigenvalues $\lambda_i^{(k)}$ of iteration k together with the residuum vector $\mathbf{r}_i^{(k)}$ (Eq. (2)). The desired vibration is selected in a root homing procedure by comparing and following the mode with largest overlap with the initial guess vector(s). The mode tracking procedure allows to exploit that the important modes of the simulated spectrum are known *a priori* without the need to calculate all $3N - 6$ vibrational frequencies, omitting all unnecessary modes which decouples the numerical effort from system size. The full Hessian matrix is not required, which is the most time consuming step in the standard quantum chemical procedure.

In Eq. 4 of the main text we assume that the "fingerprint" modes are independent, each undergoing its own fluctuations. In the mode tracking procedure both modes are naturally treated as independent normal modes (i.e. the Hamiltonian with time varying couplings is avoided). During the iterative procedure both localized normal modes are provided as guess and the mode with largest overlap is followed. By diagonalizing the small Davidson Hessian in a time-varying basis, orthogonal modes are obtained which yields the vibrational Hamiltonian $H_{nuc}(t)$ in diagonal form. The localized character on either of the two C=O groups is preserved during the dynamics

justifying the use of Eq. 4.

Mode tracking is performed over the course of the trajectories for both $C = O$ stretch vibrations of uracil with the Akira program²¹ coupled to the MOLPRO program package³ by a newly developed interface allowing for mode tracking in excited states by the supplied analytic excited state energy gradients. As initial guess the $C = O$ stretch normal mode vectors of the stationary points of the respective populated electronic state at time t are supplied. To guarantee the convergence of the desired $C = O$ modes root homing is performed by following the eigenvector with the largest overlap with the initial guess vector during the iterative procedure. The numerical derivative of the gradient of the electronic energy of the respective electronic state is evaluated for a displacement of step size 0.01 bohr²². For preconditioning an initial guess unity matrix $\mathbf{X} = \mathbf{1}$ is supplied. For the iterative procedure the convergence criteria are 0.0008 as maximum component of residuum vector $\mathbf{r}_i^{(k)}$ and 0.8×10^{-7} for the change of the maximum component of $\mathbf{r}_i^{(k)}$.

1.3 Computational Details - Semiclassical UV-Pump - IR-Probe Signal

The UV-Pump - IR-Probe signal $S_{PP}(\omega, T)$ (Eq. 4 - main text) is related to the Δ -dispersed signal $\bar{S}(\omega, T; \Delta)$ by an integration over the Δ variable (Eq. 5 - main text). $\bar{S}(\omega, T; \Delta)$ is given by

$$\begin{aligned} \bar{S}(\omega, T; \Delta) &= -\frac{2i}{\hbar^4} \int_{-\infty}^{\infty} d\tau_3 e^{-i(\omega+\Delta)(\tau_3-T)} \mathcal{E}_2(\tau_3-T) \\ &\quad \times \int_{-\infty}^{\infty} dt \theta(t-\tau_3) e^{i\omega(t-T)} \\ &\quad \times \sum_a |\mu_{ag}|^2 e^{-2\gamma_a t} \times \left(\sum_c |\mu_{ac}|^2 e^{-i \int_{\tau_3}^t \omega_{ac}(t') dt'} + \sum_d |\mu_{ad}|^2 e^{i \int_{\tau_3}^t \omega_{ad}(t') dt'} \right) \end{aligned} \quad (5)$$

The signal is calculated for a vibrational dephasing lifetime $1/\gamma_a = 325$ fs.

2 Supporting Discussion:

2.1 Electronic excited states

Quantum chemical calculations have been performed to take into account the dynamic part of the electron correlation (see SI- Table 1) which has been shown to be important for accurate vertical excitation energies in nucleobases^{9,23–25}. The calculations use *MS-MRPT2*^{26,27} level of theory and serve as a benchmark for vertical excitation energies. In all *MS-MRPT2-CAS(14/10)* calculations a levelshift $s=0.3$ ²⁸ has been applied. It turns out that the close succession of electronic states (see SI-Tab. Table 1) requires a *multi state* treatment of the dynamic electron correlation. *Single state* variants of the MRPT2 method can lead to severe artifacts, resulting in unphysical small excitation energies, as the electronic ground state and excited states are not treated in a balanced fashion.

The ground state equilibrium of the pyrimidine nucleobase uracil is a planar structure with C_s symmetry. The energy of the lowest optical accessible $\pi\pi^*$ state (A' symmetry) is 6.61 eV above the ground state on CAS(14/10) level of theory. As established for pyrimidine nucleobases^{4,9,10} the $\pi\pi^*$ state is sensitive to dynamic electron correlation effects and stabilized by ≈ 1.5 eV on MRPT2 level of theory (see SI- Table 1). On this level of theory close agreement to experimental excitation energy is obtained. The dark $n_O\pi^*$ states $1A''$ and $2A''$ are energetically close to the $\pi\pi^*$ state (5.14 and 6.69 eV respectively on CAS(14/10) level of theory, see SI- Table 1) and less sensitive to electron correlation effects. Despite the sensitivity of the $\pi\pi^*$ state to the used electronic structure method it has been shown that the CASSCF method is appropriate to describe the excited state dynamics of uracil as the relative energetics of the excited state potential energy surfaces and geometries of stationary points are reproduced well compared to higher level methods like MRCI and MRPT2^{9,10}.

2.2 Time evolution of the electronic population

Our simulations of the ensemble averaged signal $SPP(\omega, T)$ rely on populations obtained from non-adiabatic on-the-fly molecular dynamics, where the electronic structure is computed at the

Table 1: Excitation energies of uracil (in eV): the absolute energy of the electronic ground state is given in Hartree, B3LYP optimized structure with C_s symmetry; basis: 6-31G*;^a Maximum of vapor spectrum²⁹.^b CR-EOM-CCSD(T)/aug-cc-pVTZ³⁰

State	CAS(14/10)	MRPT2	Character	Exp. ^a	Theo. ^b
<i>sa4-CAS(14/10)</i>					
1A'	-412.52885	-413.60907	π		
2A'	6.61	5.07	$\pi\pi^* (H \rightarrow L)$	5.1	5.25
1A''	5.14	4.90	$n_O\pi^* (n_O \rightarrow L)$		5.00
2A''	6.69	6.37	$n_O\pi^* (n_O \rightarrow L+1)$		
<i>sa6-CAS(14/10)</i>					
1A'	-412.52735	-413.61364	π		
2A'	6.62	5.12	$\pi\pi^* (H \rightarrow L)$	5.1	5.25
3A'	7.28	6.00	$\pi\pi^* (H-1 \rightarrow L)$		
4A'	8.62	6.63	$\pi_O\pi^* (H \rightarrow L+1)$		
1A''	5.11	4.96	$n_O\pi^* (n_O \rightarrow L)$		5.00
2A''	6.69	6.40	$n_O\pi^* (n_O \rightarrow L+1)$		

CAS(14/10) level, considering the complete π system as well as both n_O lone pairs in the active space of electrons. The simulations reveal a stronger participation of the $n_O\pi^*$ state in the relaxation process compared to the population dynamics presented in Ref.^{9,10} who used a restricted CAS(10/8) level. Furthermore we observe $n_O\pi^* \rightarrow gs$ decay only for t>1ps in a minor set of two trajectories (the population dynamics until t=2 ps is given in the SI- Figure 2) which is essential for the indirect mechanism reported by Nachtigallova and coworkers⁹. As pointed out by the Lischka group³¹ a reduced active space can affect the importance of certain relaxation pathways. Asturiol *et al.* reported on thymine, based on a comparison of dynamic simulations on CASSCF level of theory and static CASPT2 calculations that the propensity of the decay of the $n_O\pi^*$ state is overestimated in the CASSCF dynamics³². Analyzing the presented population dynamics on CAS(14/10) level suggests that the $\pi\pi^* \rightarrow n_O\pi^*$ population transfer leads to a trapping of $n_O\pi^*$ population (on CAS(14/10) level of theory the $n_O\pi^*$ state is 5.14 eV above the electronic ground state, compared to 4.84 eV on CAS(10/8) level of theory⁹ at the optimized geometry of the S_0 minimum). The additional π orbital predominantly stabilizes the electronic ground state and increases its energy

gap to the $n_O\pi^*$ state. The increase in accuracy (compared to CAS(10/8)) could come at the expense that the S_3 state with $n_O\pi^*$ character facilitates and overestimates $\pi\pi^* \rightarrow n_O\pi^*$ population transfer leading to a reduced stable $\pi\pi^*$ population. Further simulations with longer propagation times and ideally considering dynamic electron correlation effects are required to quantitatively resolve the importance of the parallel relaxation mechanisms. Time resolved transient absorption measurements³³ indicate a participation of the $n_O\pi^*$ state of 10-50% (with 28 % for U) in the $\pi\pi^*$ decay, where the dark state has a lifetime of 10-150 ps, in agreement with the presented simulations. The presented IR signatures of both, the $\pi\pi^* \rightarrow n_O\pi^*$ trapping and the *diabatic* $\pi\pi_{S_2}^* \rightarrow \pi\pi_{S_1}^* \rightarrow gs$ relaxation should still be clearly detectable under these conditions allowing for a clear assignment of the individual singlet decay pathways and the participation of triplet states³⁴ on a slower timescale in time resolved UV-pump - IR-probe measurements.

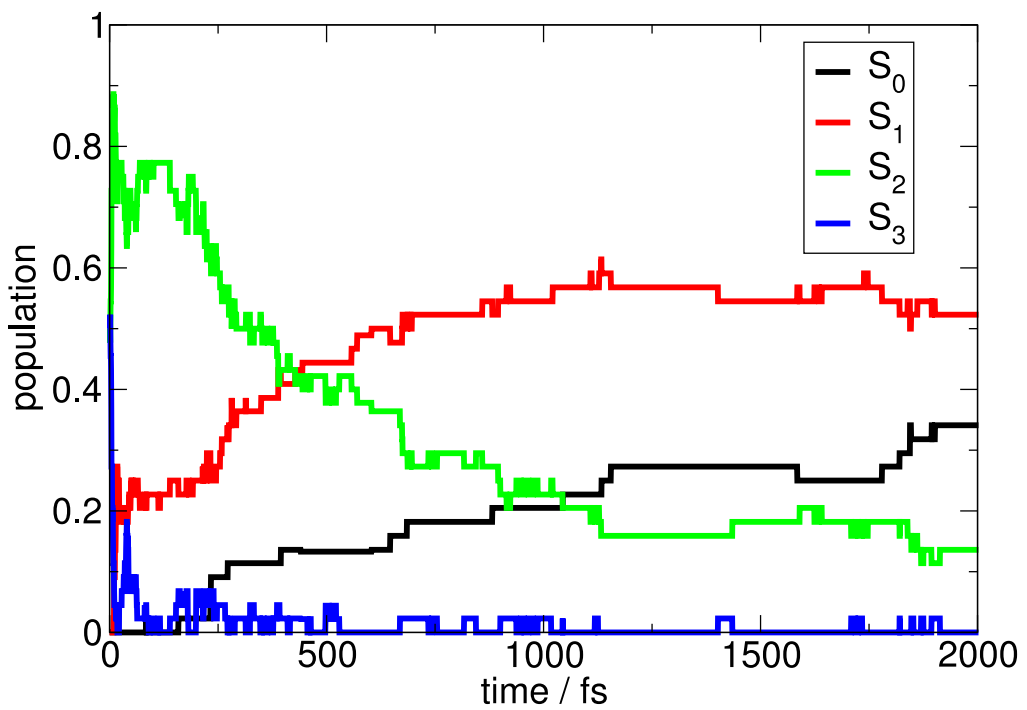


Figure 2: Time evolution of electronic populations: Mean adiabatic electronic state population averaged over 44 trajectories starting in the bright $\pi_O\pi^*$ state until $t = 2$ ps. Depending on the initial geometry the initial state is either S_2 (47.7 %) or S_3 (52.3 %)

3 Supporting Figures:

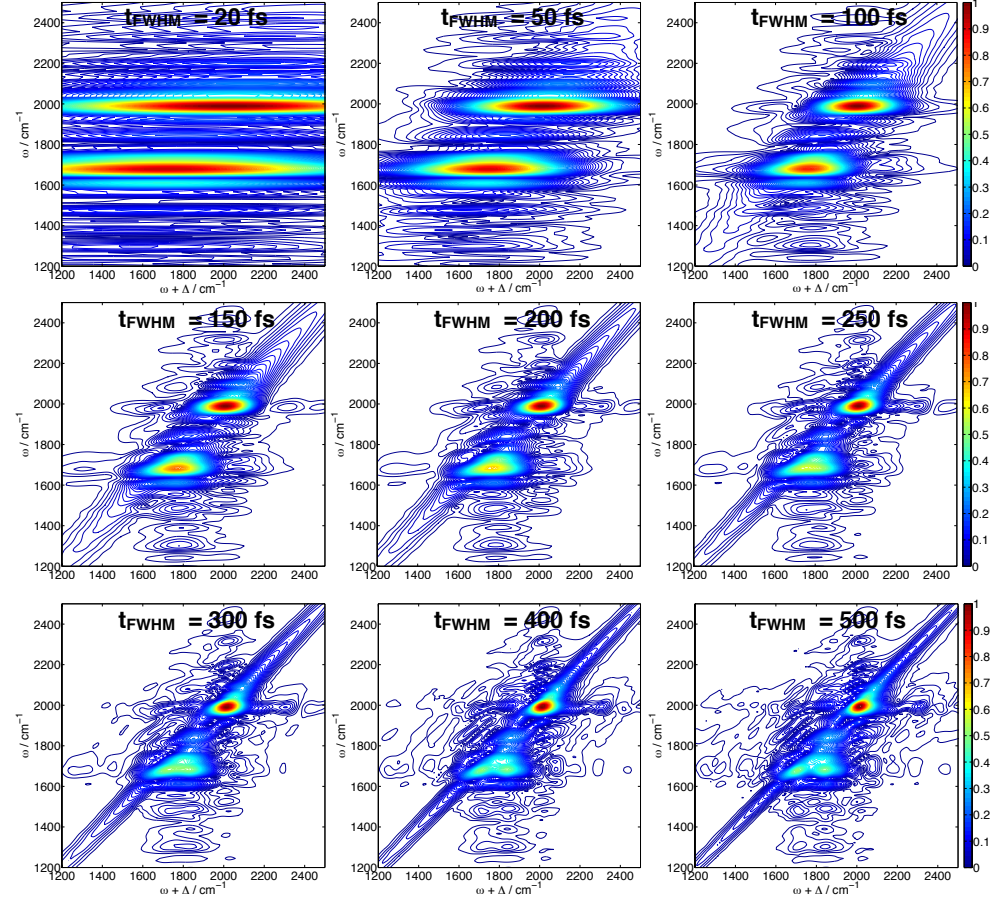


Figure 3: The Δ -dispersed signal $\bar{S}(\omega, T = 270 \text{ fs}; \Delta)$ (Eq. 5) of the trajectory of $\pi\pi^* \rightarrow n_O\pi^*$ trapping for different probe pulses characterized by t_{FWHM} as indicated.

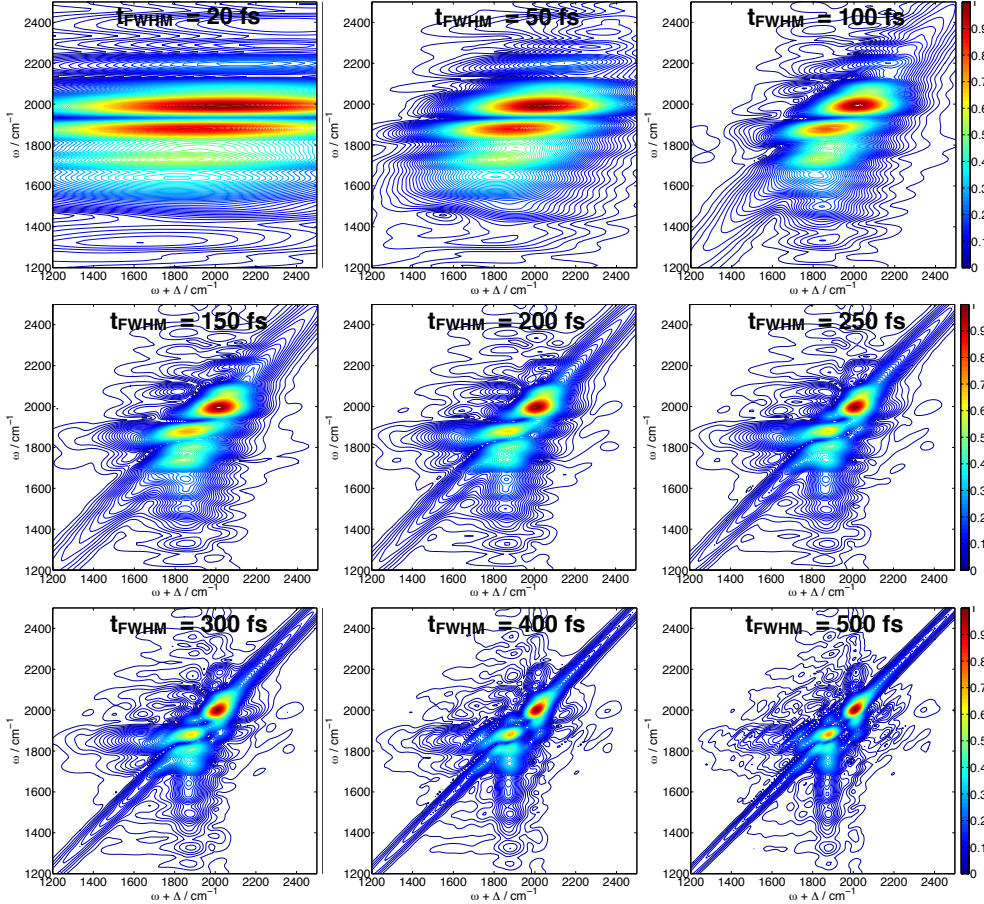


Figure 4: The Δ -dispersed signal $\bar{S}(\omega, T = 500 \text{ fs}; \Delta)$ (Eq. 5) of the trajectory of *diabatic* $\pi\pi_{S_2}^* \rightarrow \pi\pi_{S_1}^* \rightarrow \text{gs}$ relaxation for different probe pulses characterized by t_{FWHM} as indicated.

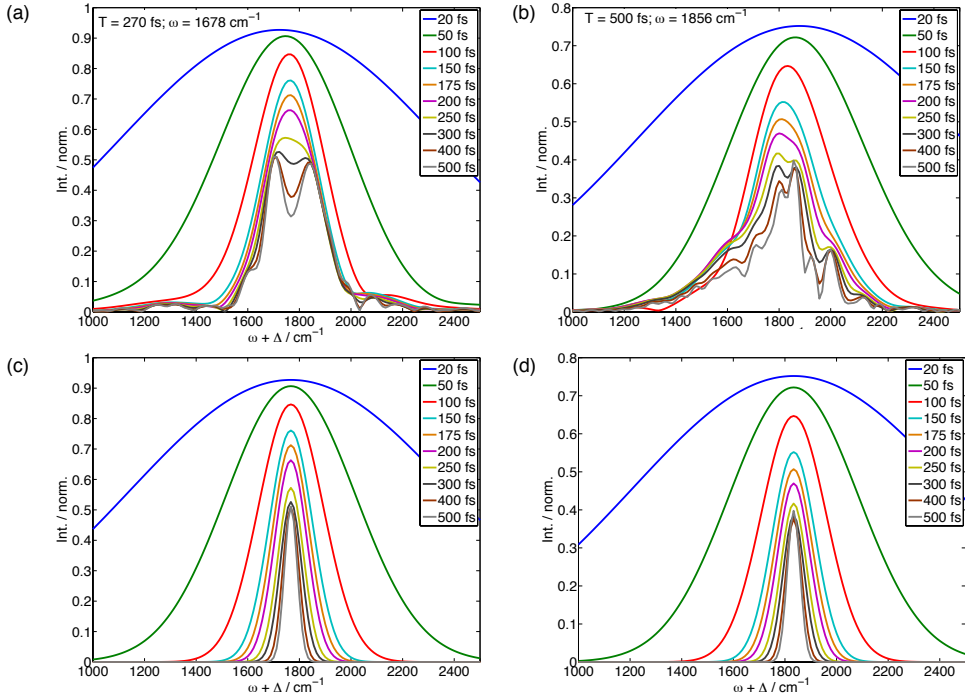


Figure 5: (a) $\bar{S}(\omega = 1678 \text{ cm}^{-1}, T = 270 \text{ fs}; \Delta)$ (Eq. 5) of the trajectory of $\pi\pi^* \rightarrow n_O\pi^*$ trapping for various probe length. (b) same as (a) but for $\bar{S}(\omega = 1856 \text{ cm}^{-1}, T = 500 \text{ fs}; \Delta)$ of the trajectory of diabatic $\pi\pi_{S_2}^* \rightarrow \pi\pi_{S_1}^* \rightarrow \text{gs}$ relaxation (c) and (d) bandwidth of used probe pulses

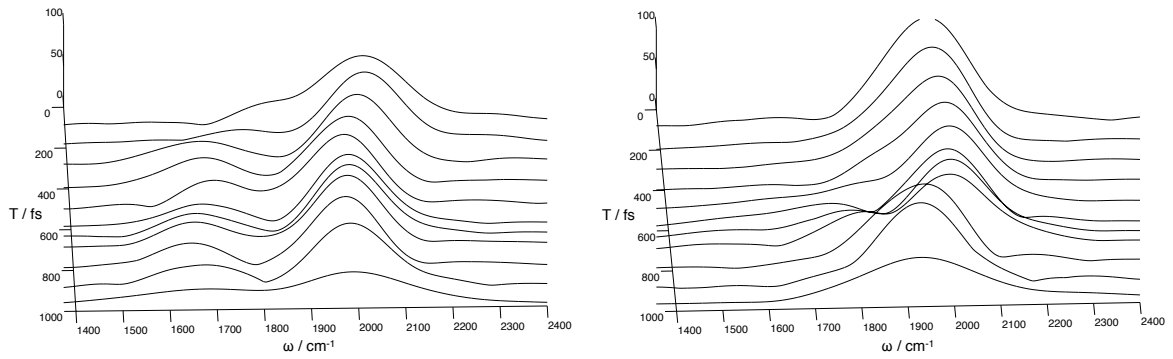


Figure 6: Pump probe signal at selected delay times T of the trajectory of $\pi\pi^* \rightarrow n_O\pi^*$ trapping (left) and of the trajectory of diabatic $\pi\pi_{S_2}^* \rightarrow \pi\pi_{S_1}^* \rightarrow \text{gs}$ relaxation (right). The time slices correspond to the contour plots depicted in Fig. ?? (a) and (e).

References

- (1) Barbatti, M.; Granucci, G.; Persico, M.; Ruckenbauer, M.; Vazdar, M.; Eckert-Maksić, M.; Lischka, H. The On-The-Fly Surface-Hopping Program System Newton-X: Application to Ab Initio Simulation of the Nonadiabatic Photodynamics of Benchmark Systems. *J. Photochem. Photobiol. A* **2007**, *190*, 228–240.
- (2) Tully, J. C. Molecular Dynamics with Electronic Transitions. *J. Chem. Phys.* **1990**, *93*, 1061–1071.
- (3) Werner, H.-J. et al. MOLPRO, Version 2006.1, A Package of Ab Initio Programs. 2006.
- (4) Fingerhut, B. P.; Oesterling, S.; Haiser, K.; Heil, K.; Glas, A.; Schreier, W. J.; Zinth, W.; Carell, T.; de Vivie-Riedle, R. ONIOM Approach for Non-Adiabatic On-The-Fly Molecular Dynamics Demonstrated for the Backbone Controlled Dewar Valence Isomerization. *J. Chem. Phys.* **2012**, *136*, 204307.
- (5) Swope, W. C.; Andersen, H. C.; Berens, P. H.; Wilson, K. R. A Computer Simulation Method for the Calculation of Equilibrium Constants for the Formation of Physical Clusters of Molecules: Application to Small Water Clusters. *J. Chem. Phys.* **1982**, *76*, 637–649.
- (6) Hammes-Schiffer, S.; Tully, J. C. Proton Transfer in Solution: Molecular Dynamics with Quantum Transitions. *J. Chem. Phys.* **1994**, *101*, 4657–4667.
- (7) Butcher, J. C. A Modified Multistep Method for the Numerical Integration of Ordinary Differential Equations. *J. Assoc. Comput. Mach.* **1965**, *12*, 124–135.
- (8) Barbatti, M.; Granucci, G.; Persico, M.; Lischka, H. Semiempirical Molecular Dynamics Investigation of the Excited State Lifetime of Ethylene. *Chem. Phys. Lett.* **2005**, *401*, 276 – 281.
- (9) Nachtigallová, D.; Aquino, A. J. A.; Szymczak, J. J.; Barbatti, M.; Hobza, P.; Lischka, H.

Nonadiabatic Dynamics of Uracil: Population Split among Different Decay Mechanisms. *J. Phys. Chem. A* **2011**, *115*, 5247–5255.

- (10) Hudock, H. R.; Levine, B. G.; Thompson, A. L.; Satzger, H.; Townsend, D.; Gador, N.; Stolow, A.; Martinez, T. J. Ab Initio Molecular Dynamics and Time-Resolved Photoelectron Spectroscopy of Electronically Excited Uracil and Thymine. *J. Phys. Chem. A* **2007**, *111*, 8500–8508.
- (11) Barbatti, M.; Aquino, A. J. A.; Szymczak, J. J.; Nachtigallová, D.; Hobza, P.; Lischka, H. Relaxation Mechanisms of UV-Photoexcited DNA and RNA Nucleobases. *Proc. Nat. Acad. Sci. USA* **2010**, *107*, 21453–21458.
- (12) Buchner, M.; Ladanyi, B. M.; Stratt, R. M. The Short-Time Dynamics of Molecular Liquids. Instantaneous-Normal-Mode Theory. *J. Chem. Phys.* **1992**, *97*, 8522–8535.
- (13) Keyes, T. Instantaneous Normal Mode Approach to Liquid State Dynamics. *J. Phys. Chem. A* **1997**, *101*, 2921–2930.
- (14) Moore, P.; Keyes, T. Normal Mode Analysis of Liquid CS₂: Velocity Correlation Functions and Self-Diffusion Constants. *J. Chem. Phys.* **1994**, *100*, 6709–6717.
- (15) Nguyen, P. H.; Stock, G. Nonequilibrium Molecular-Dynamics Study of the Vibrational Energy Relaxation of Peptides in Water. *J. Chem. Phys.* **2003**, *119*, 11350–11358.
- (16) Bastida, A.; Soler, M. A.; Zuniga, J.; Requena, A.; Kalstein, A.; Fernandez-Alberti, S. Instantaneous Normal Modes, Resonances, and Decay Channels in the Vibrational Relaxation of the Amide I Mode of N-Methylacetamide-D in Liquid Deuterated Water. *J. Chem. Phys.* **2010**, *132*, 224501.
- (17) Schreier, W. J.; Schrader, T. E.; Koller, F. O.; Gilch, P.; Crespo-Hernández, C. E.; Swaminathan, V. N.; Carell, T.; Zinth, W.; Kohler, B. Thymine Dimerization in DNA is an Ultrafast Photoreaction. *Science* **2007**, *315*, 625–629.

- (18) Schreier, W. J.; Kubon, J.; Regner, N.; Haiser, K.; Schrader, T. E.; Zinth, W.; Clivio, P.; Gilch, P. Thymine Dimerization in DNA Model Systems: Cyclobutane Photolesion is Predominantly Formed via the Singlet Channel. *J. Am. Chem. Soc.* **2009**, *131*, 5038–5039.
- (19) Haiser, K.; Fingerhut, B. P.; Heil, K.; Glas, A.; Herzog, T. T.; Pilles, B. M.; Schreier, W. J.; Zinth, W.; de Vivie-Riedle, R.; Carell, T. Mechanism of UV-Induced Formation of Dewar Lesions in DNA. *Angew. Chem. (Int. Ed.)* **2012**, *51*, 408–411.
- (20) Fingerhut, B. P.; Herzog, T. T.; Ryseck, G.; Haiser, K.; Graupner, F. F.; Heil, K.; Gilch, P.; Schreier, W. J.; Carell, T.; de Vivie-Riedle, R.; Zinth, W. Dynamics of Ultraviolet-Induced DNA Lesions: Dewar Formation Guided by Pre-Tension Induced by the Backbone. *New J. Phys.* **2012**, *14*, 065006.
- (21) Reiher, M.; Neugebauer, J. A Mode-Selective Quantum Chemical Method for Tracking Molecular Vibrations Applied to Functionalized Carbon Nanotubes. *J. Chem. Phys.* **2003**, *118*, 1634–1641.
- (22) Neugebauer, J.; Reiher, M.; Kind, C.; Hess, B. A. Quantum Chemical Calculation of Vibrational Spectra of Large Molecules—Raman and IR Spectra for Buckminsterfullerene. *J. Comput. Chem.* **2002**, *23*, 895–910.
- (23) Serrano-Andrés, L.; Merchán, M. Are the Five Natural DNA/RNA Base Monomers a Good Choice from Natural Selection? A Photochemical Perspective. *J. Photochem. Photobiol. C* **2009**, *10*, 21–32.
- (24) Kistler, K. A.; Matsika, S. Three-State Conical Intersections in Cytosine and Pyrimidinone Bases. *J. Chem. Phys.* **2008**, *128*, 215102.
- (25) Delchev, V. B.; Sobolewski, A.; Domcke, W. Comparison of the Non-Radiative Decay Mechanisms of 4-Pyrimidinone and Uracil: an Ab Initio Study. *Phys. Chem. Chem. Phys.* **2010**, *12*, 5007–5015.

- (26) Finley, J.; Malmqvist, P.-A.; Roos, B. O.; Serrano-Andrés, L. The Multi-State CASPT2 Method. *Chem. Phys. Lett.* **1998**, *288*, 299–306.
- (27) Celani, P.; Werner, H.-J. Analytical Energy Gradients for Internally Contracted Second-Order Multireference Perturbation Theory. *J. Chem. Phys.* **2003**, *119*, 5044–5057.
- (28) Roos, B. O.; Andersson, K. Multiconfigurational Perturbation Theory with Level Shift - the Cr₂ Potential Revisited. *Chem. Phys. Lett.* **1995**, *245*, 215–223.
- (29) Clark, L. B.; Tinoco, I. Correlations in the Ultraviolet Spectra of the Purine and Pyrimidine Bases. *J. Am. Chem. Soc.* **1965**, *87*, 11–15.
- (30) Epifanovsky, E.; Kowalski, K.; Fan, P.-D.; Valiev, M.; Matsika, S.; Krylov, A. I. On the Electronically Excited States of Uracil. *J. Phys. Chem. A* **2008**, *112*, 9983–9992.
- (31) Szymbczak, J. J.; Barbatti, M.; Lischka, H. Influence of the Active Space on CASSCF Nona-diabatic Dynamics Simulations. *Int. J. Quant. Chem.* **2011**, *111*, 3307–3315.
- (32) Asturiol, D.; Lasorne, B.; Robb, M. A.; Blancfort, L. Photophysics of the π, π^* and n, π^* States of Thymine: MS-CASPT2 Minimum-Energy Paths and CASSCF on-the-Fly Dynamics. *J. Phys. Chem. A* **2009**, *113*, 10211–10218.
- (33) Hare, P. M.; Crespo-Hernández, C. E.; Kohler, B. Internal Conversion to the Electronic Ground State Occurs via Two Distinct Pathways for Pyrimidine Bases in Aqueous Solution. *Proc. Nat. Acad. Sci. USA* **2007**, *104*, 435–440.
- (34) Etinski, M.; Fleig, T.; Marian, C. M. Intersystem Crossing and Characterization of Dark States in the Pyrimidine Nucleobases Uracil, Thymine, and 1-Methylthymine. *J. Phys. Chem. A* **2009**, *113*, 11809–11816.